POWERFUL H₂ LINE COOLING IN STEPHAN'S QUINTET. I. MAPPING THE SIGNIFICANT COOLING PATHWAYS IN GROUP-WIDE SHOCKS

M. E. CLUVER[1], P. N. APPLETON[2,3,9], F. BOULANGER[3], P. GUILLARD[3], P. OGLE[1], P.-A. DUC[4], N. LU[2], J. RASMUSSEN[5,10],
W. T. REACH[1], J. D. SMITH[6], R. TUFFS[7], C. K. XU[2], AND M. S. YUN[8]

[1] Spitzer Science Center, IPAC, California Institute of Technology, Pasadena, CA 91125, USA; mcluver@ipac.caltech.edu
[2] NASA Herschel Science Center, IPAC, California Institute of Technology, Pasadena, CA 91125, USA
[3] Institute d'Astrophysique Spatiale, Université Paris Sud 11, Orsay, France
[4] Laboratoire AIM, CEA/DSM - CNRS - Université Paris Diderot, DAPNIA/Service d'Astrophysique, CEA/Saclay, F-91191 Gif-sur-Yvette Cedex, France
[5] Carnegie Observatories, 813 Santa Barbara St., Pasadena, CA 91101, USA
[6] Department of Physics and Astronomy, Mail Drop 111, University of Toledo, 2801 West Bancroft Street, Toledo, OH 43606, USA
[7] Max-Planck-Institut für Kernphysik, Saupfercheckweg 1, 69117 Heidelberg, Germany
[8] Department of Astronomy, University of Massachusetts, Amherst, MA, USA

ABSTRACT

We present results from the mid-infrared spectral mapping of Stephan's Quintet using the *Spitzer Space Telescope*. A 1000 km s^{-1} collision ($t_{col} = 5 \times 10^6$ yr) has produced a group-wide shock, and for the first time the large-scale distribution of warm molecular hydrogen emission is revealed, as well as its close association with known shock structures. In the main shock region alone we find 5.0×10^8 $M_\odot$ of warm H$_2$ spread over ∼480 kpc^2 and additionally report the discovery of a second major shock-excited H$_2$ feature, likely a remnant of previous tidal interactions. This brings the total H$_2$ line luminosity of the group in excess of 10^{42} erg s^{-1}. In the main shock, the H$_2$ line luminosity exceeds, by a factor of 3, the X-ray luminosity from the hot shocked gas, confirming that the H$_2$-cooling pathway dominates over the X-ray. [Si II]34.82 μm emission, detected at a luminosity of 1/10th of that of the H$_2$, appears to trace the group-wide shock closely, and in addition, we detect weak [Fe II]25.99 μm emission from the most X-ray luminous part of the shock. Comparison with shock models reveals that this emission is consistent with regions of fast shocks (100 km s^{-1} < V_s < 300 km s^{-1}) experiencing depletion of iron and silicon onto dust grains. Star formation in the shock (as traced via ionic lines, polycyclic aromatic hydrocarbon and dust emission) appears in the intruder galaxy, but most strikingly at either end of the radio shock. The shock ridge itself shows little star formation, consistent with a model in which the tremendous H$_2$ power is driven by turbulent energy transfer from motions in a post-shocked layer which suppresses star formation. The significance of the molecular hydrogen lines over other measured sources of cooling in fast galaxy-scale shocks may have crucial implications for the cooling of gas in the assembly of the first galaxies.

Key words: galaxies: evolution – galaxies: individual (NGC 7318b, NGC 7319) – galaxies: interactions – intergalactic medium – shock waves

Online-only material: color figure

1. INTRODUCTION

Stephan's Quintet (hereafter SQ) is a strongly interacting compact group which has produced a highly disturbed intragroup medium (IGM; Xu et al. 2003, 2005) through a complex sequence of interactions and harassment (Allen & Sullivan 1980; Williams et al. 2002). This interplay has produced a large-scale intergalactic shock wave, first observed as a narrow filament in the radio continuum (Allen & Hartsuiker 1972), and subsequently detected in the X-ray (Pietsch et al. 1997; Trinchieri et al. 2005; O'Sullivan et al. 2009). The high-velocity (∼1000 km s^{-1}) collision of an intruder galaxy, NGC 7318b, with the intergalactic medium of the group (Sulentic et al. 2001; Xu et al. 2003) is believed to be responsible for the shock heating of the X-ray-emitting gas. Optical emission-line ratios and observed broad line widths provide evidence that the region is powered by strong shocks and not star formation (Xu et al. 2003; P.-A. Duc et al. 2010, in preparation).

The main elements of SQ are shown in Figure 1. Central to the system is the primary shock, as defined by the 20 cm radio continuum emission. NGC 7318b, the intruder galaxy, lies to the west of the shock, while the large Seyfert 2 galaxy (Durret 1994), lies to the east. Other members of the group are also indicated. The peculiar extranuclear star formation region, named SQ-A (Xu et al. 1999, 2003), lies at the extreme northern end of the main shock wave. NGC 7318a (west of NGC 7318b) is also a strongly interacting group member, with NGC 7317 further away from the core.

The unexpected discovery of extremely powerful, pure-rotational H$_2$ line emission from the center of the shock (Appleton et al. 2006), using the *Spitzer Space Telescope*[11] (Werner et al. 2004), has sparked intense interest in the SQ system. Warm molecular hydrogen emission was found with a line luminosity exceeding the X-ray luminosity from the shock. The mid-infrared (MIR) H$_2$ line width was resolved ($\sigma = 870$ km s^{-1}) suggesting that the H$_2$-emitting clouds carry a large bulk-kinetic energy, tapping a large percentage of the energy

---
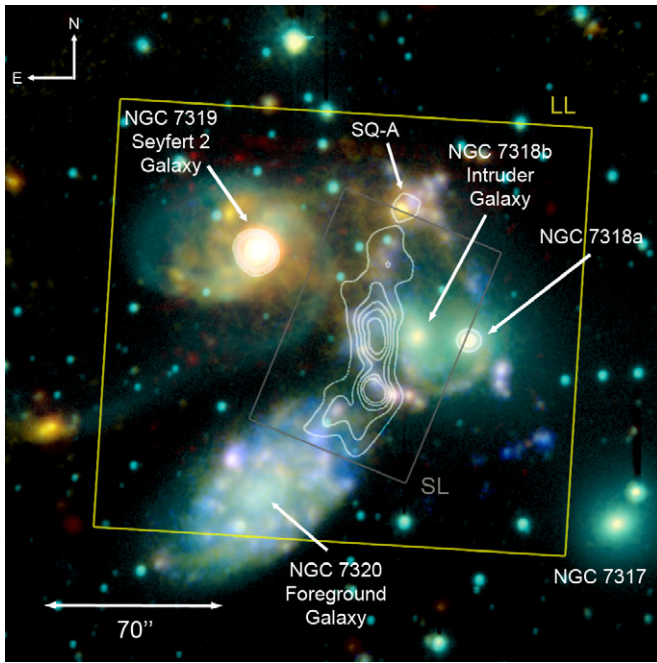
Figure 1. Schematic composite image of Stephan's Quintet consisting of a *Galex* NUV image (blue), an optical *R*-band image (cyan) from Xu et al. (1999), an IRAC 8 μm image (yellow), and an image from the 16 μm IRS peak-up array (red). The contours represent the 20 cm emission associated with the shock as obtained by the VLA (Xu et al. 2003). The boundaries of the *Spitzer* IRS spectral mapping coverage (this paper) are shown as boxes.

(A color version of this figure is available in the online journal.)

available in the shock. A recent model of SQ, involving the collision between two inhomogeneous gas flows, describes H₂ formation out of the multiphase, shocked gas, and an efficient cooling channel for high-speed shocks as an alternative to X-ray emission (Guillard et al. 2009).

Since the SQ detection, several other systems exhibiting similarly strong H₂ emission have been discovered. Ogle et al. (2007, 2010) find that a large subset of the local 3CR radio galaxies has extremely dominant MIR rotational H₂ lines, often seen against a very weak thermal continuum. The low active galactic nucleus (AGN) and star formation power are insufficient to drive the MIR H₂ emission. Mechanical heating driven by the radio jet interaction with the host galaxy interstellar medium (ISM) is the favored mechanism. In addition, total H₂ luminosities in the range 10^{41}–10^{43} erg s^{-1} have been detected in some central cluster galaxies out to $z \sim 0.3$ (Egami et al. 2006, G. de Messieres 2009, private communication) and in filaments in clusters (Hatch et al. 2005). The study of nearby prototypes may provide valuable insight into the nature of these more distant systems. The large scale ($\sim$30 kpc) of the SQ shock is well-suited for such a study.

In this Paper I, we extend the single-pointing observations of Appleton et al. (2006) to full spectral maps of SQ using the Infrared Spectrograph (IRS) instrument on the *Spitzer Space Telescope* (hereafter *Spitzer*). In Paper II, we will present detailed two-dimensional excitation maps of the H₂ emission across the face of the X-ray-emitting shock, and compare them with models. In addition, several other papers are being prepared by our team in which the relationship between the UV/X-ray emission and emission from dust will be discussed.

In Section 2, we present our observations and data reduction methods. In Section 3, we discuss the mapping results for various detected lines. In Sections 4–6, we present our discussion on the

properties of the system, and in Section 7 the implication for galaxy formation has been presented. In Section 8, we present our conclusions. Additional material is included as appendices, with a discussion on NGC 7319 in Appendix A, and a reanalysis of the high-resolution MIR spectrum of the shock, as well as reanalysis of the X-ray data presented in Appendices B and C, respectively.

Throughout this paper, we assume a systemic velocity of $v = 6600$ km s^{-1} for the group, corresponding to a distance of 94 Mpc with $H_{o} = 70$ km s^{-1} Mpc^{-1}.

2. OBSERVATIONS AND DATA REDUCTION

MIR spectroscopy of the shock region in SQ was obtained using the IRS instrument (Houck et al. 2004) onboard *Spitzer*. Observations were done in low-resolution mapping mode, using the short-low ($R \sim 60$–127; 5.2–14.5 μm) and long-low ($R \sim 57$–126; 14.0–38.0 μm) modules and taken on 2008 January 11 and 2007 December 10, respectively. Figure 1 displays the outline of the areas observed superimposed on a composite image of the group.

The short-low (SL) spectral mapping consists of two separate, partially overlapping maps, centered north and south on the X-ray emission associated with the shock. The map was constructed with 23 steps of 2$''$8 (0.75 $\times$ slit width) perpendicular to the slit and one parallel step of 7$''$2. Observations consisted of 60 s integrations with 5 cycles per step.

The long-low (LL) module was used to map an area of $\sim$2$'$8 $\times$ 3$'$2 using 21 steps of 8$''$0 (0.75 $\times$ slit width) perpendicular to the slit and a parallel step of 24$''$0. An integration time of 120 s was used with 3 cycles per step.

Primary data reductions were done by the Spitzer Science Center (SSC) pipeline, version S17.0.4 and S17.2.0 for SL and LL, respectively, which performs standard reductions such as ramp fitting, dark current subtraction, and flat-fielding. Background subtraction for LL data was performed by subtracting dedicated off-source observations, with the same observing mode, taken shortly after the mapping sequence. In the case of SL, where for scheduling reasons the dedicated "off" observations were too far away in time to be optimal, backgrounds were generated from observations at the periphery of the map that contain no spectral line signatures.

Examination of the pipeline products showed that the stray-light-corrected images (that account for potential spillover from the peak-up arrays onto the SL1/2 spectral apertures) contained wavelength-dependent overcorrections in some of the images, seemingly due to a high background of cosmic rays during the SL portion of the mapping. To negate this effect, the alternative flat-fielded images (also available from the science pipeline) that are uncorrected for crosstalk and stray-light removal were used. It was determined that after background subtraction, any uncorrected stray light in the SL spectral extraction areas was unmeasurable at the <2%–3% level. Thus, stray-light correction was unnecessary, and the resulting basic calibrated data (BCD) images used were of better quality than the standard BCDs.

For all modules, individual frames for each pointing were median-combined and obvious "bad" pixels were replaced using customized software that allows for manual "average" replacement. The spectra were assembled into spectral cubes for each module using the software tool, CUBISM (Smith et al. 2007). Further bad pixel removal was performed within CUBISM. Spectral maps were generated by making continuum maps on either side of a feature and subtracting the averaged continuum map from the relevant emission-line map.

One-dimensional spectra were further extracted from the data cubes using matched apertures.

Broadband images at 16 and 24 μm were obtained with the *Spitzer* IRS blue peak-up imager (PUI) and the Multiband Imaging Photometer for *Spitzer* (MIPS) instrument. The PUI was obtained in a 5×5 map with 3 cycles of 30 s duration each on 2007 December 10. The MIPS instrument (Rieke et al. 2004) on *Spitzer* obtained 24 μm imaging of SQ on 2008 July 29, achieving a spatial resolution of $\sim$6″. Primary data reduction was done by the SSC science pipeline (version S18.0.2) run through the MOPEX software, and for the MIPS image a smooth two-dimensional polynomial background was further removed to correct for a large-scale background gradient. *Spitzer* IRAC 3.6, 4.5, 5.8, and 8.0 μm data of SQ (PI: J. R. Houck) were obtained from the SSC archive; these were reduced using science pipeline version S18.0.2. The final mosaics have a pixel scale of 0″.61.

3. RESULTS

3.1. The Molecular Hydrogen Distribution

The pure rotational transitions of molecular hydrogen can be excited by several mechanisms. These include far-ultraviolet (FUV) induced pumping, and possible additional collisional heating, of the H_2 in photodissociation regions (PDRs) associated with star formation (e.g., Black & van Dishoeck 1987; Hollenbach & Tielens 1997), hard X-rays penetrating and heating regions within molecular clouds, which in turn excite H_2 via collisions with electrons or hydrogen atoms (Lepp & McCray 1983; Draine & Woods 1992) and finally collisional excitation of H_2 due to acceleration produced by shocks (e.g., Shull & Hollenbach 1978). The pure rotational MIR line ratios are not especially good diagnostics for distinguishing between these mechanisms, since all three mechanisms discussed can lead to well thermalized level distributions of lower level rotational states. The rotational H_2 emission lines do, however, allow us to trace gas at different temperatures and compare with model predictions (this will be the main emphasis of Paper II). Higher level transitions 0-0 S(3)–S(5) tend to trace warmer gas, whereas the S(0) and S(1) lines are sensitive to the "coolest" warm H_2.

Although the line ratios themselves cannot be used directly as shock diagnostics, in SQ the distribution of large-scale X-ray and radio emission, plus optical emission-line diagnostics, provides strong evidence that the giant filament seen in Figure 1 is the result of a strong shock. In Appleton et al. (2006), this fact was used to reveal the surprising association of detected H_2 emission with the shock. However, in this paper, we can make a more definitive association of the emission with the shock by means of spectral maps.

The spectral cubes were used to extract maps of all the pure rotational emission lines of molecular hydrogen that were detected, namely the 0-0 S(0) 28.22 μm, S(1) 17.03 μm, S(2) 12.28 μm, S(3) 9.66 μm, S(4) 8.03 μm, and S(5) 6.91 μm lines. Specific intensity contour maps of these lines are presented in Figure 2 overlaid on a *R*-band image of the region from Xu et al. (1999). The S(0) and S(1) lines were mapped by the LL modules, while S(2)–S(5) transitions were mapped by the SL modules of the IRS. As indicated in Figure 1, the SL observations were concentrated on the main shock to provide high signal-to-noise (S/N) measurements there. As a result, these maps do not fully cover SQ-A or NGC 7319. We note that the S(4) line at 8.03 μm (Figure 2(e)) is faint and also suffers

from contamination from the polycyclic aromatic hydrocarbon (PAH) bands at 7.7 μm and 8.6 μm.

The contours indicate powerful, widespread emission running north–south (NS) along the shock ridge (see Figure 1). In addition, we detect strong emission from the star-forming region, SQ-A, as well as associated with NGC 7319. We discuss further details of the AGN-like MIR emission lines from NGC 7319 in Appendix A.

Figures 2(a)–(d) reveal a new H_2 structure running eastward from the "main" shock ridge. In what follows, we refer to this feature as the "bridge." This structure is observed faintly in the *Chandra* (Trinchieri et al. 2003) and *XMM-Newton* (Trinchieri et al. 2005) X-ray images and detected as faint Hα emission by Xu et al. (2003), but is not strong in radio continuum images.

As is evident in Figure 2, there is distinct variation in the distribution of the warm H_2 emission. The brightest 0-0 S(0) emission (Figure 2(a)) appears to be concentrated toward the north of the shock, whereas the 0-0 S(1) transition emission (Figure 2(b)) appears more concentrated toward the center. The S(0) and S(1) maps demonstrate that the H_2 in the bridge terminates in a large clump a few arcsecs west of the nucleus of the Seyfert 2 galaxy NGC 7319, and in a small detour to the north (especially in the S(1) map which has the highest S/N).

The S(2)–S(5) lines clearly show that the warm H_2 emission breaks into clumps in the shock. Despite the limited coverage compared to the LL mapping, the base of the "bridge" is visible and SQ-A is partially covered. SQ-A is fully covered by the SL2 module (because of fortuitous "off observation" coverage) and hence the S(5) emission line reveals that in SQ-A the H_2 emission is also clumpy.

The molecular-line maps provide considerable information about the excitation of the H_2 along and across the X-ray shock, but these discussions will be deferred to a full two-dimensional modeling of the H_2 excitation in Paper II (P. N. Appleton et al. 2010, in preparation). Instead we shall limit ourselves to global properties of the H_2 here. In Section 4, we shall present spectra of some selected regions of the emission and discuss a global excitation diagram for the shock.

To further demonstrate the close connection between the H_2 emission and the main global shock wave in SQ, we now consider the distribution of warm H_2 in relation to the X-ray and radio emission. Figures 3(a) and (b) show the S(0) and S(3) contours overlaid on an *XMM-Newton* X-ray image (Trinchieri et al. 2005) of SQ. The warm molecular hydrogen is distributed along the length of the main north–south X-ray shock ridge and along the "bridge," demonstrating the remarkable projected co-existence of hot X-ray plasma ($10^6 < T < 10^7$ K) and warm H_2 ($10^2 < T < 10^3$ K). Although the H_2 appears to follow the X-ray, there are subtle differences. The cooler S(0) line has emission concentrated to the north and follows the X-ray less closely compared to the warmer S(3) line. The S(3) line exhibits a clear correspondence to the X-ray, notably at the center of the shock, where we find peaks at both wavelengths. Thus, the region of greatest shock heating, as traced by the stronger X-ray emission, appears to correspond to the higher J H_2 transitions, perhaps implying a causal connection. The intergalactic star formation region SQ-A is essentially absent in X-ray emission, as seen in Figure 3(a), but is strongly detected in H_2.

We find a similar picture in the radio continuum (Figures 3(c) and (d)), with the S(0) line demonstrating correspondence with the main shock, but dominated by emission in the north where we observe less powerful radio emission. The S(3) (and S(2)–
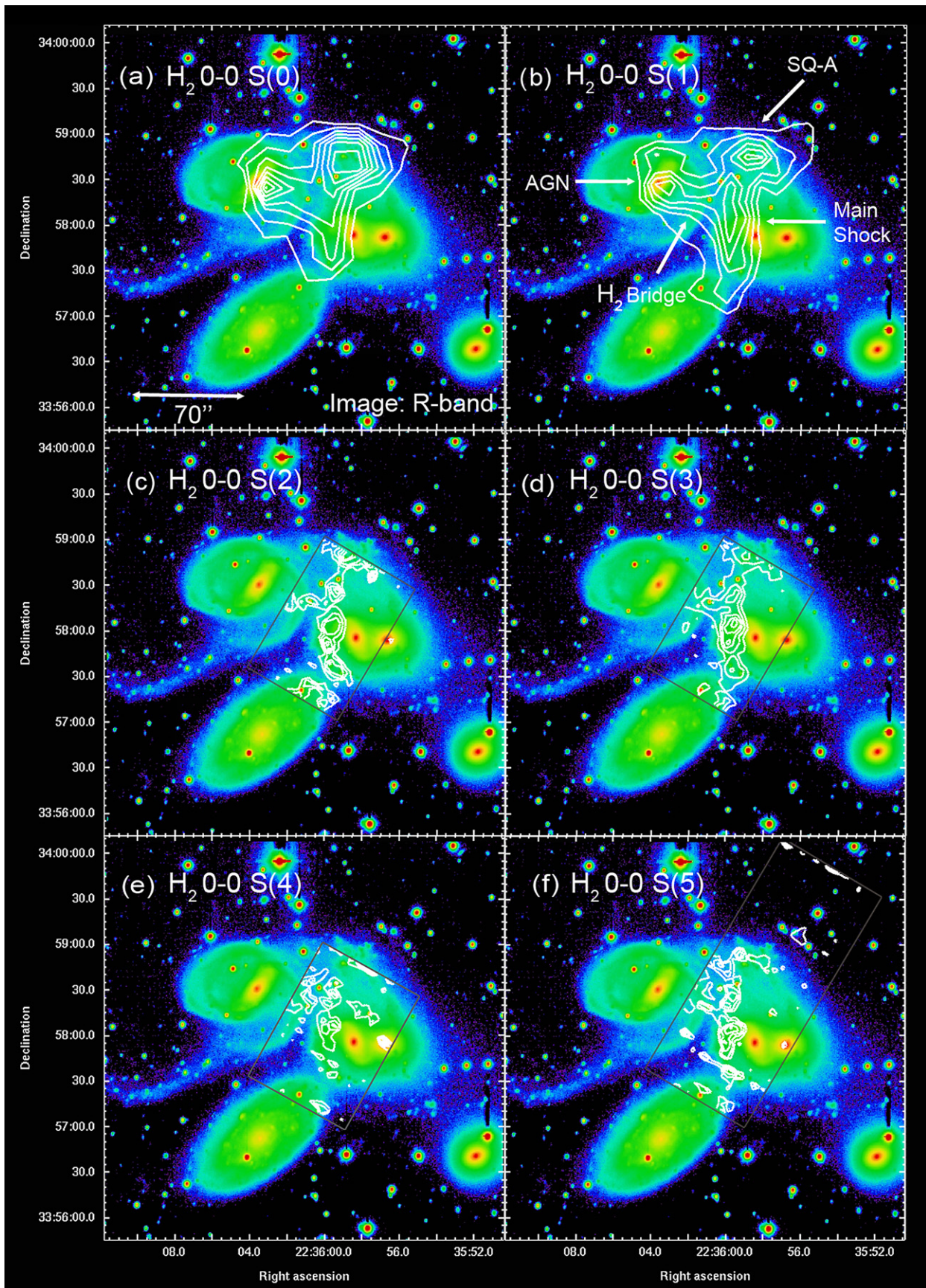
Figure 2. Large-scale distribution of warm H_2 in Stephan's Quintet with each detected 0-0 transition overlaid on an R-band image from Xu et al. (1999). The gray box indicates the limit of the SL module coverage. Contour levels are as follows (all in units of MJy sr^{-1}): (a) 0.1, 0.14. 0.19, 0.28, 0.32, 0.37, 0.41, 0.46, 0.5, (b) 0.3, 0.53, 0.75, 0.98, 1.2, 1.43, 1.65, 1.88, 2.1, (c) 0.3, 0.4, 0.5, 0.6, 0.7, (d) 0.25, 0.42, 0.58, 0.75, 0.92, 1.08, 1.25, (e) 0.11, 0.19, 0.27, 0.36, 0.44, 0.52, 0.6, and (f) 0.3, 0.46, 0.61, 0.77. 0.93, 1.09, 1.24, 1.4. The SL coverage for (f) is larger due to incorporating the "parallel mode" SL2 slit observations from the "off-target" positions when SL1 mapping observations were the primary observing mode.
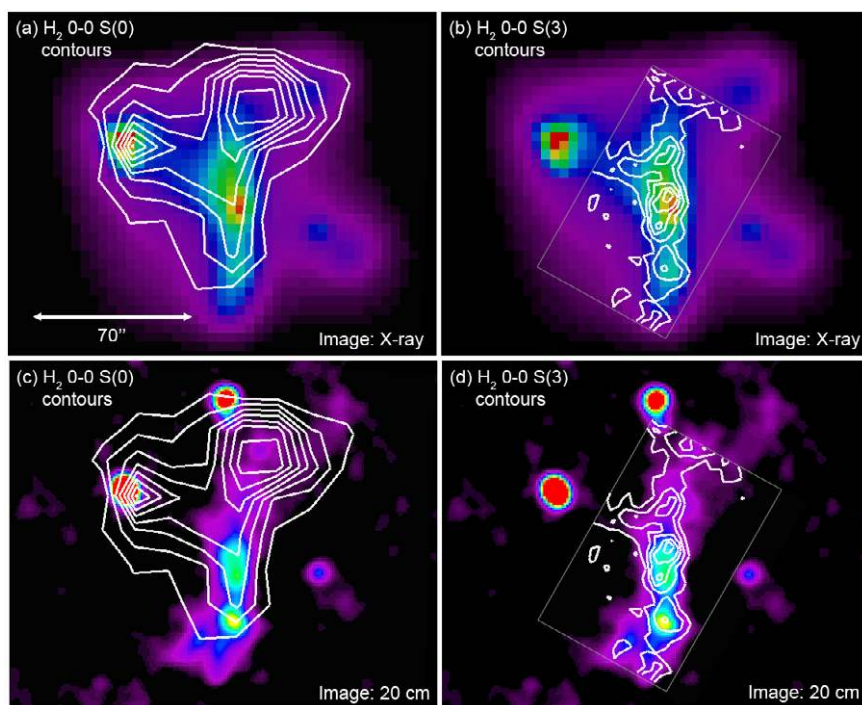
Figure 3. X-ray image from *XMM-Newton* (Trinchieri et al. 2005) in the 1.5–2.5 keV band with (a) H$_2$ S(0) contours and (b) H$_2$ S(3) contours overlaid. Also shown are 1.4 GHz radio continuum images from the VLA (Xu et al. 2003) with (c) H$_2$ S(0) contours and (d) H$_2$ S(3) contours overlaid. Contours levels are as in Figure 2.
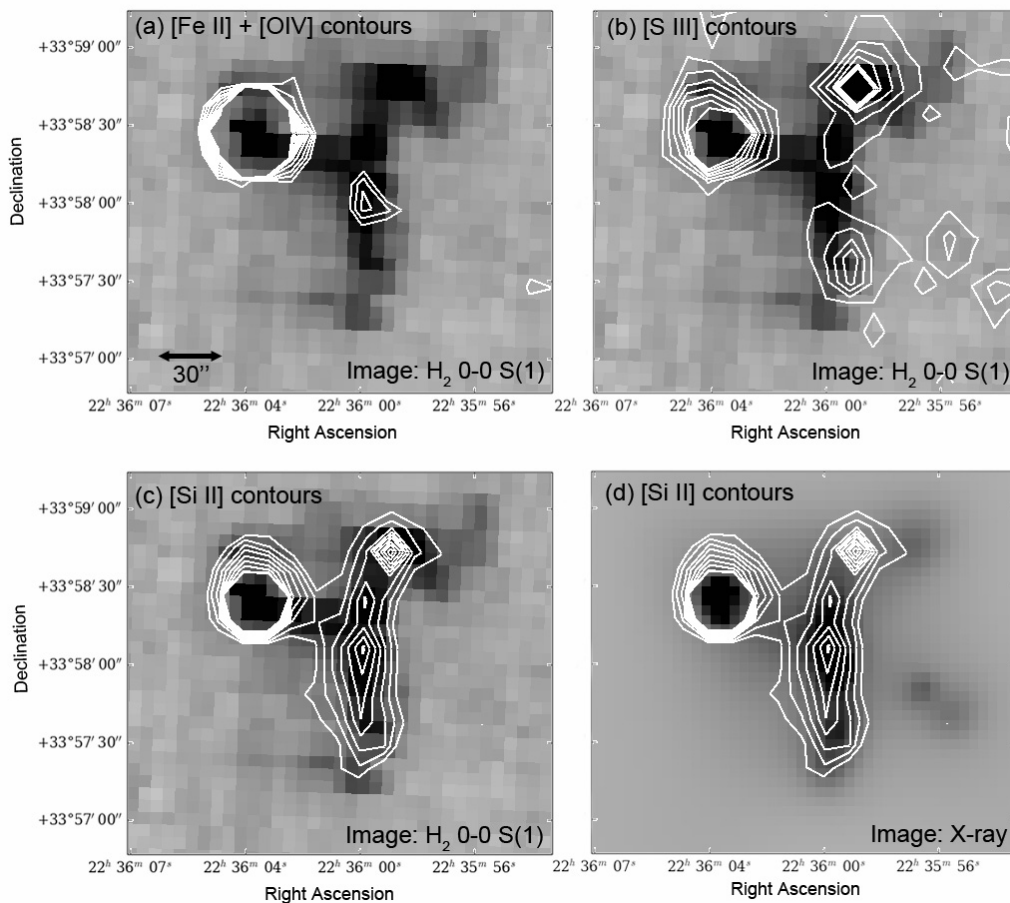
Figure 4. Fine structure emission ([Fe II]25.99 μm and [O IV]25.89 μm blend, [S III]33.48 μm and [Si II]34.82 μm) compared to the distribution of H$_2$ S(1) emission. Also shown are [Si II]34.82 μm contours compared to X-ray 0.5–1.5 keV emission. Contour levels are as follows (all in units of MJy sr^{-1}): (a) 0.08, 0.1, 0.13, 0.15, 0.165, 0.18, 0.2, 0.22, 0.23, 0.25, (b) 0.2, 0.33, 0.47, 0.6, 0.73, 0.87, 1.0 with (c) and (d) having levels of 0.5, 0.66, 0.83, 0.99, 1.15, 1.31, 1.48, 1.6, 1.8. These levels are chosen to best show the intensity of emission associated with the shock and do not reflect the full intensity range for NGC 7319.

see Figure 2(c)) line presents a much tighter correlation with regions of the shock that are more radio luminous than the lower J transitions. The radio emission is quite likely sensitive to the most compressed regions of the shock where cosmic-ray particles are accelerated more strongly (Helou & Bicay 1993; Appleton et al. 1999), whereas the brightest X-ray patches are likely due to the fastest regions of the shock (Guillard et al. 2009). As already mentioned, the "bridge" emission is detected only faintly in the X-ray and is weak or absent at radio continuum wavelengths. This noticeable difference compared to the main shock likely implies that the conditions that give rise to strong synchrotron emission in the main shock are absent in the bridge.

3.2. Shock-related Fine-structure Line Emission

Emission from fine-structure lines provides key diagnostics that trace the interplay between the various constituents of the shocked interstellar medium. In Appleton et al. (2006), the spectra were limited to the very core of the shock and only weak emission was detected from all but two metal lines, namely [Ne II]12.81 μm and [Si II]34.82 μm (these data have been reanalyzed and are presented in Appendix B). In this section, we discuss the spatial distribution of emission from the [Fe II]25.99 μm, [O IV]25.89 μm, [S III]33.48 μm, [Si II]34.82 μm, [Ne II]12.81 μm, and [Ne III]15.56 μm lines.

In Figure 4, we present the specific intensity contours of the [Fe II]25.99 μm and [O IV]25.89 μm blend, [S III]33.48 μm and [Si II]34.82 μm emission lines.

Given the low spectral resolution of the SL and LL modules of *Spitzer*, we cannot distinguish between emission from [Fe II]25.99 μm and [O IV]25.89 μm. However, except in the direction of the Seyfert II galaxy NGC 7319, the emission near 26 μm seen in Figure 4(a) is likely to be pure [Fe II] with little contamination from [O IV] as there is no evidence from the spectra of high-excitation emission from the IGM in SQ. For example, [O IV] has an excitation potential of 56 eV (compared to 7.9 eV of [Fe II]), and yet Appleton et al. (2006) have shown that the [Ne III]/[Ne II] ratio is low suggesting low-excitation conditions for the ions in the shock, further supported in Section 5. Assuming that, apart from toward NGC 7319, [Fe II] dominates the [Fe II]+[O IV] complex, we detect faint emission from [Fe II]25.99 μm at the location of the center of the shock (as defined by the X-ray "hotspot" in Figure 3(a)). The energetic requirements for shocks to produce strong [Fe II] emission are usually present in *J* shocks, while the ion abundance in *C* shocks is low in comparison (Hollenbach & McKee 1989). We will discuss the production of [Fe II] in the shock in Section 6.2.

The [S III]33.48 μm distribution is presented in Figure 4(b). This fine-structure line acts as a strong tracer of H II regions (Dale et al. 2006), and we observe emission from SQ-A and from other regions of star formation in the south (see Section 3.3). In the primary shock region, the distributions of [Fe II] and [S III] are anticorrelated.

In strong contrast to the weak [Fe II] emission, there is copious [Si II]34.82 μm emission (Figure 4(c)), which follows the S(1) distribution closely with respect to the primary shock, as mapped by X-ray emission (Figure 4(d)).

Although [Si II] is commonly found in normal H II regions, we will demonstrate below that, apart from in SQ-A, the strong silicon emission does not correlate with regions of strong PAH emission (tracing star formation) in SQ, but instead closely follows the H₂ and X-ray (shock) distributions. [Si II] acts as an efficient coolant of X-ray-irradiated gas and is predicted to

be one of the top four cooling lines under these circumstances (Maloney et al. 1996). We will discuss the excitation of [Si II] in the shock in Section 6.2.

[Ne II]12.81 μm (with an ionization potential of 21.6 eV) is also represented in the shock, as shown in Figure 5(a), although it is also emitted from some H II regions associated with star formation, such as SQ-A and the star-forming region south of NGC 7318b (see Section 3.3). The [Ne III]15.56 μm contours (with an ionization potential of 41 eV) are shown in Figure 5(b) and are associated with excitation in the shock, as well as from regions of star formation (see Section 3.3). The higher ionization line of [Ne III] is much weaker in the shock ridge, but regions of emission correspond closely to peaks seen for the H₂ S(3) line. The [Ne II] emission, however, exhibits clearly extended emission with regions of greatest luminosity matching those seen for the H₂ S(3) line. The [Ne II] emission suggests excitation from the shock, with [Ne III] found at the location of the center of the shock, similar to what is observed for [Fe II].

### 3.3. Star Formation Tracers and Dust Emission in SQ

Previous observations and spectroscopy of SQ (Xu et al. 2005) have determined that there are some regions of star formation associated with the spiral arms of the intruder galaxy NGC 7318b. We discuss in this section how these regions, which have a different spatial distribution from the shocked gas, are correlated with the PAH emission we detect in the IRS spectra.

In Figure 6(a), there is a strong correlation between the 11.3 μm PAH distribution (from the IRS cube) superimposed on a near-UV (NUV) image from *Galex* (Xu et al. 2005), which maps the UV emission from hot stars associated with weak star formation from the system. This correlation suggests that the PAH molecules are excited by star formation. A similar close correlation is shown in Figure 6(b) where we overlay the 11.3 μm contours on the IRAC 8 μm band, which is dominated by the 7.7 and 8.6 μm features. It is noticeable, however, that regions with strong 11.3 μm emission in the shock do not appear similarly strong at 8 μm. This point will be addressed in Section 6.4.

We compare the 11.3 μm PAH map to the distribution of warm dust in Figure 6(c), using the MIPS 24 μm map of SQ. Again, it is clear that there is a good correlation between the PAH emission and the thermal dust, most of which seems only poorly correlated with the shock ridge. The lack of conspicuous star formation in the ridge was also observed by Xu et al. (2003).

The main point we emphasize here is that the dust, PAH, and UV emission appear to be associated with previously known star formation regions, and no additional star formation is observed in the shock; this can be seen in Figure 6(d) showing the H₂ 0-0 S(1) emission overlaid on an IRAC 8 μm image. There is little correspondence between the H₂ emission in the shock and 8 μm (hot dust plus PAH) image. This is important because it implies that there is very little triggered star formation in the molecular gas associated with the shock-excited H₂.

Figure 6(c) demonstrates that there is only faint dust emission at 24 μm from the shock ridge. The presence of dust in the shock is required in the model of Guillard et al. (2009) to explain the formation of H₂ behind the shock, and we do observe evidence of depletion onto dust grains (see Section 6.2). Thus, the faint 24 μm emission could be the result of destruction of very small grains (VSGs), with only larger grains surviving, or indicate that the grains are cold and radiating more strongly at longer wavelengths, where *Spitzer* has the least spatial resolution. A
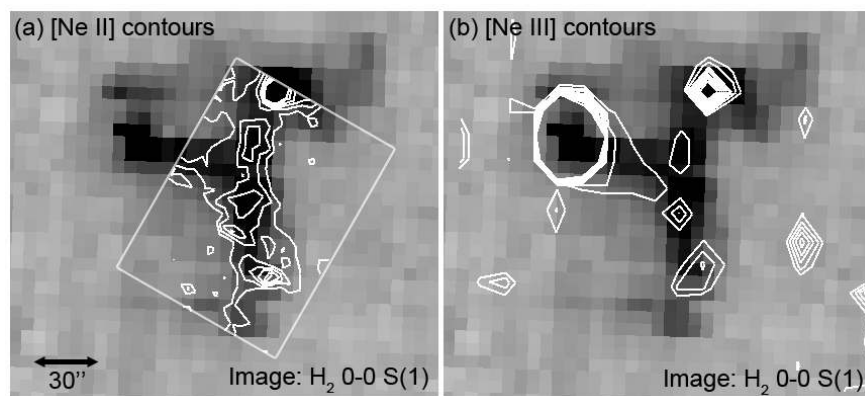
Figure 5. [Ne II]12.81 μm and [Ne III]15.56 μm emission compared to the distribution of H$_2$ S(1) emission. Contour levels are as follows (in units of MJy sr^{-1}): (a) 0.22, 0.4, 0.57, 0.75, 0.92, 1.1 and (b) 0.06, 0.08, 0.1, 0.13, 0.16, 0.18, 0.2, 0.23, 0.25.
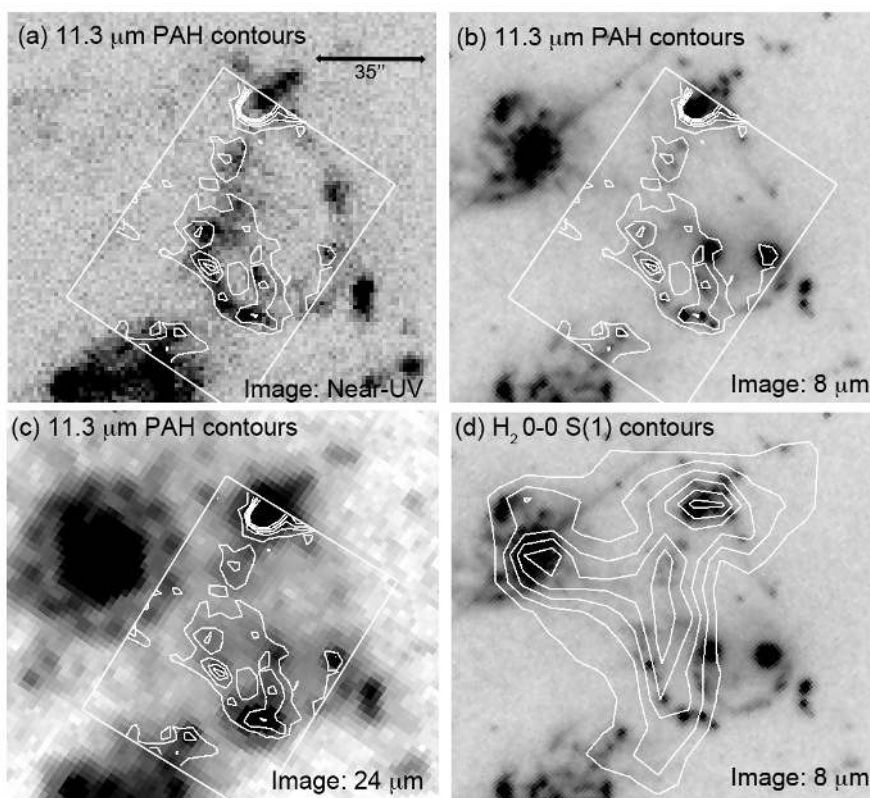
Figure 6. Dust as tracers of star formation. The 11.3 μm PAH contours overlaid on (a) the NUV, (b) an 8 μm image, and (c) a 24 μm image. By comparison, the H$_2$ 0-0 S(1) contours show little correlation with the 8 μm image (as shown in d). Contour levels are as follows (in units of MJy sr^{-1}): (a), (b), and (c) are 0.2, 0.35, 0.5, 0.65, 0.8. Contour levels for (d) are as in Figure 2(b).

more detailed description of the dust and faint PAH emission in the SQ group (including results from MIPS 70 μm imaging) is discussed in separate papers (Guillard et al. 2010; Natale et al. 2010, in preparation). Guillard et al. (2010) show that the IR emission in the shock is faint due to dust being heated by a relatively low intensity UV radiation field and determine a Galactic PAH/VSG abundance ratio in this region.

A more complete understanding of the likely existence of cool dust in the shock will require higher angular resolution and a broader wavelength coverage than that achieved by *Spitzer*.

Despite the faintness of emission from the main shock, the 24 μm map presents a new result, which was less obvious in previous studies, namely that the dominant regions of star formation in SQ lie not in the galaxies themselves, but in two strikingly powerful, almost symmetrically disposed regions at

either end of the shock. The region to the north is the well-studied SQ-A, but the region to the south (which we refer to as 7318b-south) is also very powerful, and both regions lie at the ends of the shock, as defined by the H$_2$ distribution. This may not be a coincidence, and we will discuss this further in Section 6.1.

The [Ne II]12.81 μm, [Ne III]15.56 μm, and [S III]33.48 μm fine-structure lines, as mentioned above, are also tracers of star formation in SQ as these lines are often associated with H II regions. The [Ne II]12.81 μm emission appears to follow *both* the H$_2$ and the star formation regions (see Figure 5(a)), appearing more extended in the south than the corresponding H$_2$ emission and flaring out where star formation regions, especially 7318b-south, are observed optically, and through PAH emission (see Figure 6).
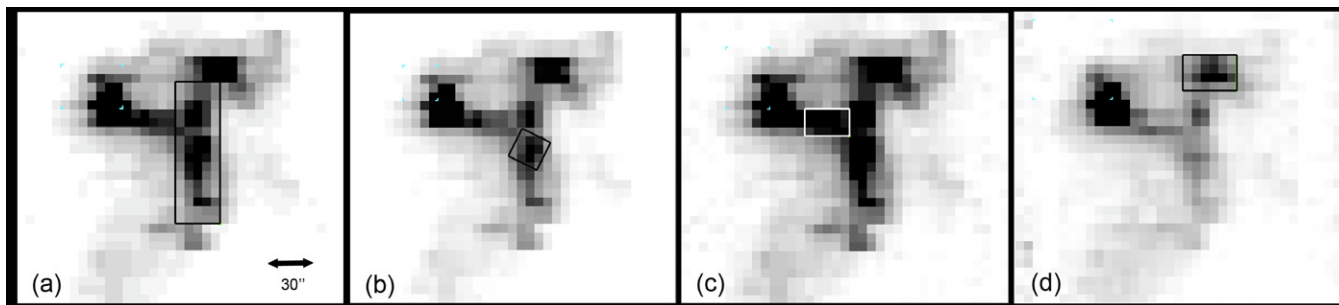
Figure 7. Rectangular sub-regions extracted from the main components of the SQ shock system overlaid on the H$_2$ 0-0 S(1) line emission. (a) The main shock region centered on 22^{h}35^{m}59^s.6, +33°58′05″.7. (b) A region in the main shock centered on 22^{h}35^{m}59^s.97, +33°58′23″.3 and chosen to have limited contamination from star-forming regions in SQ. (c) Extraction of the H$_2$ "bridge" feature centered on 22^{h}36^{m}0^s.14, +33°58′23″.3. (d) An extraction of the SQ-A star-forming region centered on 22^{h}35^{m}58^s.85, +33°58′50″.4.

4. GLOBAL PROPERTIES OF THE MOLECULAR HYDROGEN IN SQ

The warm molecular hydrogen in SQ follows the X-ray distribution in the main shock and in the "bridge" structure. This might suggest that the molecular hydrogen is excited directly by the X-ray heating. However, we will show that the H$_2$ emission exceeds by at least a factor of 3 the X-ray luminosity from the various shocked filaments, thus ruling out direct X-ray excitation from the shock.

To measure the strength of the H$_2$ emission, we extract spectra from various rectangular sub-areas of SQ which are defined in Figure 7. The spectra were extracted from CUBISM cubes built from each IRS module and joined to make a continuous spectrum—no scaling was necessary to join the spectra.

Figures 7(a)–(c) indicate the spectral extraction regions of the main NS shock, a subregion of the shock and a characteristic part of the "bridge." The shock subregion is chosen to be just north of the center of the shock, avoiding regions contaminated by star formation in the intruder. Spectra for these extractions are shown in Figures 8(a)–(c). All three spectra share the common property that they are dominated by molecular hydrogen emission. The shock subregion (Figure 8(b)), unlike Figure 8(a), is less contaminated by the star-forming regions discussed in the previous section. The MIR continuum of the main shock appears stronger than the shock subregion indicating stronger emission from warm dust; this is likely the result of contamination from star-forming regions in the main shock extraction. The bridge exhibits a similarly weak continuum emission compared to the shock subregion.

Figure 8(b) includes photometry from the IRAC bands, 16 μm PUI, and MIPS-24 μm image superimposed on the IRS spectrum. These are useful to probe conditions in the shock, in particular star formation (see Section 6.4). Stellar light in the extraction area, from an extended spiral arm of NGC 7318b, produces contamination of the shock spectrum, visible as continuum emission shortward of 6 μm, in both Figures 8(a) and (b).

There exists a striking similarity between the MIR spectrum of all three regions, showing powerful H$_2$ lines and low excitation weak emission from fine-structure lines. Also the PAH emission observed in the spectra of the shock regions, and in the region of the "bridge" in the IRAC 8 μm image (Figure 6(b)), appears weak. This confirms that these properties, observed in the Appleton et al. (2006) observations of the shock core, extend to both the full extent of the main shock and the "bridge." This and the fact that the "bridge" has similar X-ray properties to the main shock (see later) suggest that the bridge

is a "scaled-down" version of the main shock. The weaker radio continuum emission at this location is significant. One possibility that the "bridge" is older than the main shock and the cosmic rays compressed in it have diffused away will be discussed further in Paper II. Thus, the new IRS observations seem to suggest that more than one large-scale group-wide shocks are present in the group. This could be the result of previous tidal interactions and imply multiple shock-heating events have taken place in SQ, consistent with what is seen in the X-ray (O'Sullivan et al. 2009).

Figures 7(d) and 8(d) present the extraction region and spectrum of SQ-A, the extragalactic star-forming region. In this case, although H$_2$ lines are still strong, a rising continuum and an increase in the strength of the metal lines relative to the H$_2$ are consistent with a spectrum that is increasingly dominated by star formation—a result which is already known from previous optical observations (Xu et al. 2003).

Line fluxes for all the H$_2$ and metal lines in the spectra discussed above are presented in Tables 1 and 2, respectively. We estimate the luminosity emitted from the H$_2$ lines in the main aperture shown in Figure 8(a). The emission from the 0-0 S(1) line, alone can be calculated from Table 1 (for $D = 94$ Mpc), to be 2.3×10^{41} erg s^{-1}. Summing the emission measured in the observed lines for the main shock (0-0 S(0) through S(5) lines) and including an extra 28% emission from unobserved lines (see model fit to excitation diagram below) yield a total H$_2$ line luminosity from the main shock of 9.7×10^{41} erg s^{-1}. This phenomenal power in the molecular hydrogen lines dwarfs by a factor of 10 the next brightest MIR line, which is [Si II]34.82 μm with a line luminosity of $L_{\text{Si II}} = 0.85 \times 10^{41}$ erg s^{-1}.

Figure 9 presents the excitation diagram of the low-J 0-0 H$_2$ transitions for the main shock extraction. The points are well fit by a model including three temperature components ($T_1 = 158 \pm 6$ K, $T_2 = 412 \pm 4$ K, and $T_3 = 1500 \pm 200$ K). It is likely that in reality, many different temperature components are present in the shock, and the three-temperature fit is only an approximation. However, it does allow us to provide an estimate of the total mass of warm H$_2$ of $(5.0 \pm 1) \times 10^8 M_\odot$. Temperature T_2 is more uncertain than formally represented by the fit because it depends on the value of the S(4) flux, which may be systematically too low due to PAH contamination (see Figure 9). In Paper II, we will present a more complete two-dimensional map of the excitation of the H$_2$ in SQ and explore variations in the shape of the excitation diagram along and across the shock in more detail.

Our observations have shown that H$_2$ is the dominant line coolant in the MIR. However, how does it compare with the most important coolant in high-speed shocks, namely the X-ray
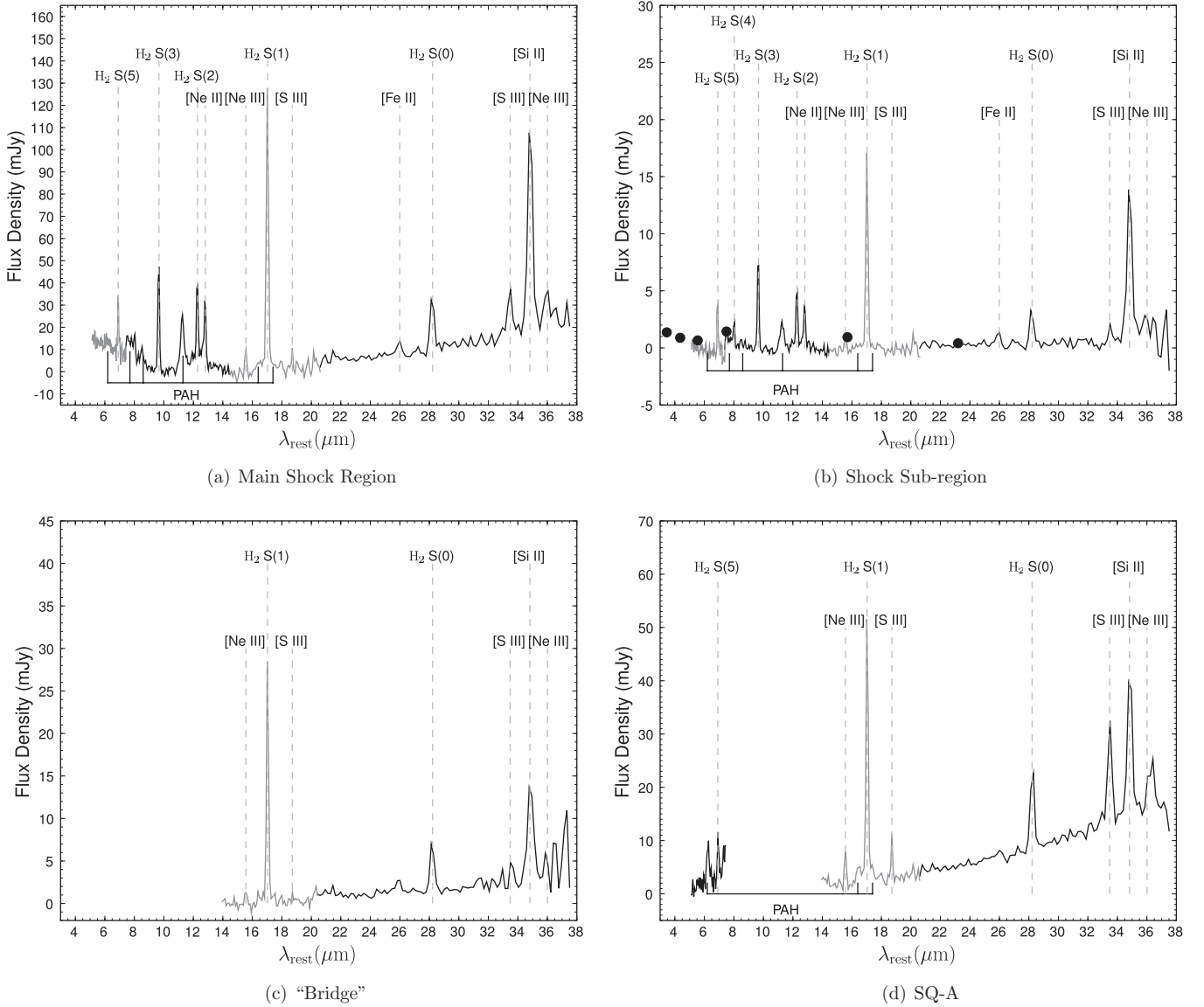
Figure 8. Extracted spectra (low resolution) of the regions shown in Figure 7, combining all IRS modules with coverage. The key emission features are labeled with measurements and sizes of extraction areas given in Table 1, which provides the H_2 line fluxes, and Table 2 listing the metal line measurements. The shock subregion (shown in b) includes the IRAC, 16 μm PUI, and 24 μm MIPS measurements for the same area. The 16 μm flux is 0.939 ± 0.047 mJy, which includes emission from the 17.03 μm H_2 line covered by the filter, while the 24 μm flux is 0.408 ± 0.046 mJy; photometry was performed using a circular aperture with no aperture correction applied to compensate for contamination from the surrounding emission. The corresponding IRAC fluxes are 1.362 ± 0.068, 0.885 ± 0.045, 0.659 ± 0.036, and 1.434 ± 0.073 mJy for the 3.6, 4.5, 5.8, and 8.0 μm bands, respectively. The extraction of SQ-A (shown in d) also has coverage from the SL2 module due to the orientation of the IRS during the SL1 observation.

Table 1
Observed H_2 Line Fluxes in units of 10^{-17} W m^{-2}

Target Region	Aperture (arcsec^2)	H_2 0-0 S(0) $\lambda 28.22\,\mu$m	H_2 0-0 S(1) $\lambda 17.03\,\mu$m	H_2 0-0 S(2) $\lambda 12.28\,\mu$m	H_2 0-0 S(3) $\lambda 9.66\,\mu$m	H_2 0-0 S(4) $\lambda 8.03\,\mu$m	H_2 0-0 S(5) $\lambda 6.91\,\mu$m
Main shock	2307	3.09 ± 0.19	23.05 ± 0.26	9.10 ± 0.38	22.76 ± 0.84	2.5 ± 1.0	14.1 ± 0.7
Shock sub-region	242	0.36 ± 0.03	3.13 ± 0.02	1.47 ± 0.08	3.60 ± 0.08	1.04 ± 0.15	2.37 ± 0.30
Bridge	413	0.72 ± 0.04	4.94 ± 0.09	...	...	...	...
NGC 7319	1302	2.06 ± 0.26	11.00 ± 0.48	...	...	...	...
SQ-A	671	1.83 ± 0.05	8.8 ± 0.13	...	...	...	3.7 ± 0.93

Note. Upper limits are the 3σ values calculated from the RMS and the expected line profile width.

emission? Appleton et al. (2006) suggested that the H_2 emission was stronger than the X-ray emission at the shock center. This can now be evaluated over much of the inner SQ group.

We present a complete reanalysis of the *XMM-Newton* observations of SQ using the latest calibrations (see Appendix C for full details) in order to determine the fluxes and luminosities of the X-ray emission to match our spectral extractions. The results indicate the striking dominance of the H_2 line luminosities compared with the X-ray emission from the same regions. For the main shock, the X-ray "Bolometric" flux of $L_{X(0.001-10\,keV)} =$

Table 2
Observed Fine Structure Line Fluxes in Units of 10^{-17} W m^{-2}

Target Region	[Ne II] $\lambda 12.81\,\mu$m	[Ne V] $\lambda 14.32\,\mu$m	[Ne III] $\lambda 15.56\,\mu$m	[S III] $\lambda 18.71\,\mu$m	[Ne V] $\lambda 24.32\,\mu$m	[Fe II]+[O IV] $\lambda 25.99+25.89\,\mu$m	[S III] $\lambda 33.48\,\mu$m	[Si II] $\lambda 34.82\,\mu$m
Main shock	5.31 ± 0.30	<0.9	1.94 ± 0.39	0.76 ± 0.13	<0.14	1.07 ± 0.10	1.87 ± 0.15	8.59 ± 0.27
Shock sub-region	1.04 ± 0.09	<0.18	0.15 ± 0.06	<0.12	<0.14	0.15 ± 0.03	0.13 ± 0.02	1.23 ± 0.04
Bridge	. . .	. . .	0.39 ± 0.04	<0.1	<0.15	0.29 ± 0.04	<0.22	1.1 ± 0.1
NGC 7319	. . .	2.89 ± 0.64	9.47 ± 0.29	2.81 ± 0.40	1.56 ± 0.39	10.9 ± 0.27	5.0 ± 0.42	9.24 ± 0.49
SQ-A	. . .	<0.8	1.29 ± 0.16	0.87 ± 0.06	<0.18	<0.17	1.54 ± 0.10	2.3 ± 0.16

Note. Upper limits are the 3σ values calculated from the RMS and the expected line profile width.
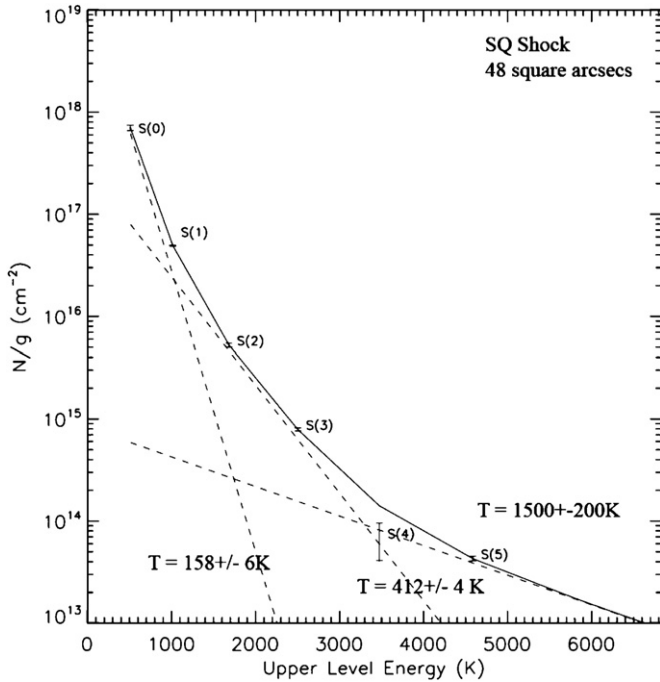
Figure 9. Excitation diagram of the main shock region in SQ. The ordinate (N/g) represents the column density divided by the statistical weight of the rotational state.

2.8×10^{-13} erg s^{-1} cm^{-2} corresponds to 2.95×10^{41} erg s^{-1}, or $L(\mathrm{H}_2)/L_{\mathrm{X}(0.001-10\,\mathrm{keV})} = 2.9$. This is a lower limit since we have not attempted to remove the contribution to the main shock aperture of an extended group-wide X-ray component upon which the emission from the shock lies. Therefore, it is likely that the H$_2$ line luminosity dominates over the main shock X-ray gas by a factor $\geqslant 3$. Similar calculations can be done for the other regions for which H$_2$ spectra have been extracted. For example, in the "bridge" region which we have already indicated has many of the same characteristics as the main shock, we find $L(\mathrm{H}_2)/L_{\mathrm{X}(0.001-10\,\mathrm{keV})} = 2.5$. These values demonstrate that throughout the extended regions of SQ, the molecular hydrogen cooling pathway dominates over the X-ray in this shocked system. This is a very significant result, upturning the traditional view that X-ray emission always dominates cooling in the later stages of evolution in compact groups of galaxies.

5. EMISSION-LINE DIAGNOSTICS

The fine-structure flux ratios (see Table 2) can be used to probe the conditions within the extracted regions of SQ. The [Si II] 34.82 μm/[S III]33.48 μm ratio provides an indication of the sources of excitation within the system. As mentioned previously, [S III] is mainly a tracer of H II regions, whereas enhanced

[Si II] emission can be generated via several mechanisms, including thermal excitation by X-rays (XDRs), or in shocks. In the main shock, the [Si II] 34.82 μm/[S III]33.48 μm ratio of $\sim$4.59 is high compared to, for example, both normal galaxies ($\sim$1.2) and AGNs ($\sim$2.9) in the *Spitzer* Infrared Nearby Galaxy Sample (SINGS) sample (Dale et al. 2006). However, this large aperture is contaminated by star formation emission from SQ-A and the intruder galaxy. A better measure is given by the smaller shock subregion, where the [Si II] 34.82 μm/[S III]33.48 μm ratio is $\sim$9.5. Thus, it is clear that the [Si II] emission is well outside the normal range of values, even for local well-studied AGNs. Using the upper limit found for [S III] 33.48 μm in the "bridge" structure, we find a ratio of >5—again values well outside the range of normal galaxy disk emission. Indeed, these high values are typical of galactic supernova remnants where shock excitation is well determined (e.g., Neufeld et al. 2007; Hewitt et al. 2009). We will argue in the following section that silicon is being ionized in regions experiencing fast shocks 100 km s^{-1} < V_s < 300 km s^{-1} and depleted onto dust grains. The [Fe II] 26.0 μm/[Si II] 34.82 μm ratio for the main shock and subregion ($\sim$0.12) is in agreement with values found by Neufeld et al. (2007) for their sample of supernova remnants.

For the extragalactic star-forming region SQ-A, [Si II] 34.82 μm/[S III] 33.48 μm is $\sim$1.49, only slightly higher than the average of $\sim$1.2 found for star-forming regions in the SINGS sample (Dale et al. 2006); another indication that SQ-A is dominated by star formation.

In star-forming galaxies, the [Ne III] 15.56 μm/[Ne II] 12.81 μm ratio can be used as a measure of the hardness of the radiation field as it is sensitive to the effective temperature of the ionising sources. In the main shock, we find a value of $\sim$0.36 which would be considered typical compared to those found in starburst systems, which range from $\sim$0.03 to 15 (Verma et al. 2003; Bernard-Salas et al. 2009), and in supernovae remnants ranging from $\sim$0.07 to 1.24 (Neufeld et al. 2007; Hewitt et al. 2009). The shock subregion has a ratio of only $\sim$0.14 indicating a lower intensity radiation field north of the shock center. However, it is clear from its spatial distribution relative to the 8 μm and H$_2$ emission that most of the neon is not originating from star formation, and so shocks are an obvious source of excitation.

The [Ne II] 12.81 μm/[Ne III] 15.56 μm ratio can be used to estimate the shock velocity using the MAPPINGS shock model library of Allen et al. (2008). In the main shock, this ratio corresponds to shock speeds between 100 and 300 km s^{-1} (using pre-shock densities of 0.01 cm^{-3} < n < 100 cm^{-3} and magnetic parameter $B/n^{0.5} = 1$ and 3.23—the nominal equipartition value[12]). We do, however, have contamination from star-forming regions in the main shock and cannot disentangle this emission

_____

[12] See Allen et al. (2008).
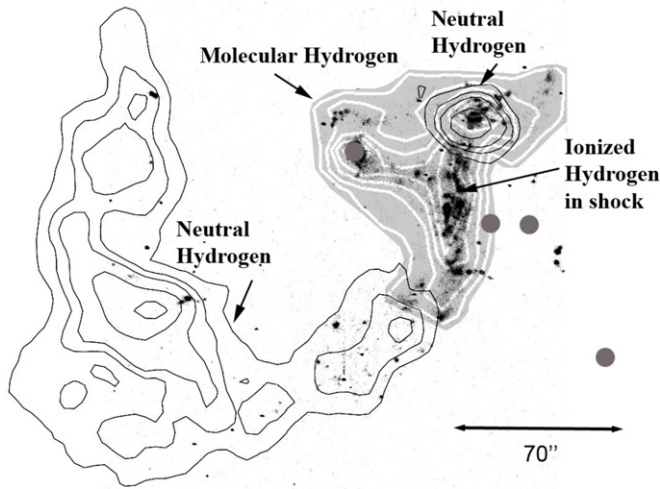
Figure 10. Schematic diagram of the H I distribution in SQ, from Williams et al. (2002), and the H$_\alpha$ emission (Xu et al. 1999), with the H$_2$ 0-0 S(1) emission overlaid. The gray dots represent the locations of the core galaxies in the group as shown in Figure 1.

from that produced in the shock. To address this, we use the [Ne II] 12.81 μm and [Ne III] 15.56 μm maps to mask areas associated with star formation (see Section 3.3) and determine a lower limit for the [Ne II] 12.81 μm/[Ne III] 15.56 μm ratio in the shock of ∼4.54. This value corresponds to a shock velocity of ∼150 km s^{-1}.

The average electron density is determined from the [S III]18.71 μm/[S III]33.48 μm (two lines of the same ionization state) ratio. For SQ-A, we find a ratio of ∼0.56, and in the main shock ∼0.41. This corresponds to an electron density of 100–200 cm^{-3} (Martín-Hernández et al. 2002) for both, i.e., in the low-density limit for this diagnostic (Smith et al. 2009).

6. THE GROUP-WIDE SHOCKS

6.1. Origin of the H$_2$ and X-ray Emission

Our observations have shown that the molecular hydrogen and X-ray-emitting plasma appear to follow a similar distribution, and we have ruled out the possibility that this is a consequence of X-rays heating the H$_2$, since the H$_2$ has the dominant luminosity. How then can we explain the similar distributions? Are these results consistent with the hypothesis that the shock is formed where the intruding galaxy NGC 7318b collides with a preexisting tidal filament of H I drawn out of NGC 7319 in a previous interaction with another group member (Moles et al. 1997; Trinchieri et al. 2003)?

This basic mechanical picture appears plausible as can be seen in Figure 10 which shows that the H$_2$ distribution "fills in" the gap in the H I tidal tail as observed by the Very Large Array (VLA; Williams et al. 2002). The implication is that the H I has been converted into both a hot X-ray component and a warm H$_2$ component by the collision of the intruder with the now missing H I.

Part of the puzzle of how this high-speed (V_s ∼ 700–1000 km s^{-1}) shock can lead to both X-ray and very strong molecular line emission is presented in a model by Guillard et al. (2009). The high-speed collision of NGC 7318b with the H I filament (assumed to be composed of a multiphase medium) leads to multiple shocks passing through and compressing denser clumps (which become dusty nucleation sites for H$_2$ formation) as opposed to the lower density gas, which is shock heated to X-ray temperatures. The H$_2$ therefore forms in denser

clouds experiencing slower shocks. Thus, the co-existence of both hot X-ray gas and cooler molecular material is a natural consequence of the multiphase medium of the pre-shocked material.

Modeling of the H$_2$ excitation by Guillard et al. (2009) demonstrates that the emission can be reproduced by low velocity (∼5–20 km s^{-1}) magnetohydrodynamic (MHD) shocks within the dense ($n_H > 10^3$ cm^{-3}) H$_2$ gas. The denser clouds survive long enough to be heated by turbulence in the hot gas component, tapping into the large available kinetic energy of the shock. This picture is consistent with both the broad H$_2$ line width (870 km s^{-1}) measured in IRS high-resolution spectrometer observations of Appleton et al. (2006) and the velocity center of the warm H$_2$ (based on new IRS spectral calibrations, see Appendix B) which places the gas at intermediate velocities between the intruder and the group IGM. Both of these measurements are consistent with H$_2$ being accelerated in a turbulent post-shocked layer.

Intermediate pre-shock densities and post-shock temperatures result in regions of H I and H II that have cooled, but where the dust content has been destroyed (Guillard et al. 2009). Preexisting giant molecular clouds (GMCs) which may have been embedded in the H I gas would be rapidly compressed and collapse quickly, thus forming stars. This mechanism, proposed for SQ-A by Xu et al. (2003), might also apply to 7318b-south. However, if this was the case, it would have to explain why two such GMCs happened to be positioned at the extreme ends of the current shock—an unlikely coincidence. More probable, however, is that the geometry of the shock somehow favors the collapse of clouds at the ends of the shock—perhaps in regions where the turbulent heating is less efficient.

6.2. Origin of [Fe II] and [Si II] Emission

As outlined above, the combination of emission detected in the shock region of SQ can be understood in terms of a spectrum of shock velocities. The fastest shock velocities (V_s ∼ 600 km s^{-1}) are associated with the lowest density preshock regions and the post-shock X-ray-emitting plasma. These are fast J shocks and represent a discontinuous change of hydrodynamic variables and are often dissociative (Hollenbach & McKee 1989). C shocks have a broad transition region such that the transition from pre-shock to post-shock is continuous and are usually non-dissociative (Draine et al. 1983). The lowest velocity shocks associated with the turbulent H$_2$ emission are ∼5–20 km s^{-1} C shocks (Guillard et al. 2009). Xu et al. (2003) find optical emission-line ratios consistent with shock models that do not include a radiative precursor (Dopita & Sutherland 1995).

The [Fe II]25.99 μm emission associated with the shock region in SQ is relatively weak, but coincides with the most energetic part of the shock as traced by the X-rays (Figure 4). We also detect abundant [Si II]34.82 μm emission associated with the main shock.

Silicon and iron have very similar first and second ionization potentials. Their first ionization potentials (7.9 and 8.15 eV for Fe and Si, respectively) are lower than that of hydrogen, but their second ionization potential is higher (16.19 and 16.35 eV). The MIR [Fe II] and [Si II] line emission observed from the SQ shock could thus arise from predominantly neutral, as well as ionized gas. We discuss the contribution from the ionized gas using the [Fe II](25.99 μm)/[Ne II](12.81 μm) and [Si II](34.82 μm)/[Ne II](12.81 μm) line ratios. The high [Ne II](12.81 μm)/[Ne III](15.56 μm) MIR line ratio (see
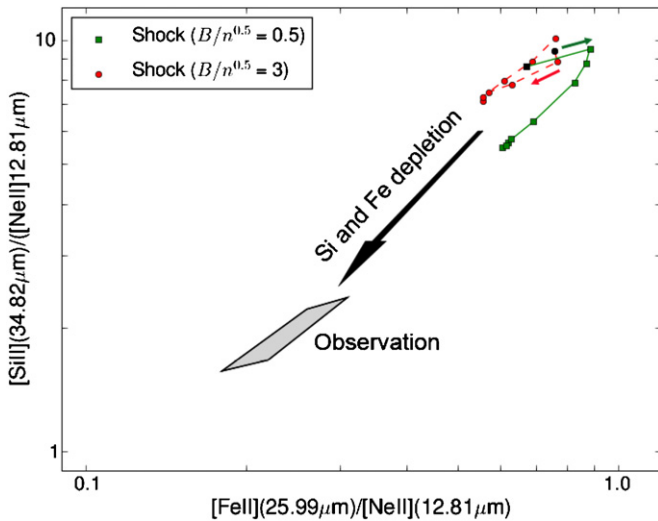
Figure 11. Line ratios measured in the main SQ shock of the [Ne ɪɪ](12.8 μm), [Fe ɪɪ](26.0 μm), and [Si ɪɪ](34.8 μm) lines are compared with shock calculations from Allen et al. (2008). The model values cover a shock velocity range of 100–300 km s^{-1} with a gas density of 1 cm^{-3} and two values of the magnetic parameter $B/n^{0.5}$ = 0.5 (green square) and 3 (red circles). The black symbols represent the 100 km s^{-1} values, and the arrows indicate the direction of increasing velocity (in steps of 25 km s^{-1}). The gray area indicates the range of line ratios, [Si ɪɪ]/[Ne ɪɪ] and [Fe ɪɪ]/[Ne ɪɪ], determined from observations (as discussed in Section 5). The ratios are lower than the model values which we interpret as evidence for Si and Fe depletion onto dust grains.

Section 5) implies that [Ne ɪɪ] is the dominant ionization state of Ne in the SQ shock. Unlike Fe and Si, Ne is not much depleted on dust (Simpson et al. 1998). Because the [Ne ɪɪ] 12.81 μm line has a high critical density ($n_e = 4.3 \times 10^5$ cm^{-3}; Ho & Keto 2007), the neon line strength scales with the emission measure of the ionized gas.

The optical line emission from the SQ shock is discussed in detail in Xu et al. (2003). The high values of the [O ɪ](6300 Å) and [N ɪɪ](6584 Å) lines to Hα line ratios are evidence of shock ionization. The optical [S ɪɪ](6716 Å/6731 Å) line ratio as well as the MIR [S ɪɪɪ] line ratio correspond to the low density limit (see Section 5), and comparison with the shock models of Allen et al. (2008) constrains the pre-shock gas density to be about 1 cm^{-3} or smaller.

In Figure 11, we indicate the region (in gray) corresponding to the observed MIR ratios (using the upper and lower limits determined for the [Ne ɪɪ]12.81 μm line emission as discussed in Section 5). For comparison, the expected emission from the shock models of Allen et al. (2008) are displayed for

a pre-shock gas density of 1 cm^{-3} and two values of the magnetic parameter, $B/n^{0.5}$ = 0.5 and 3. For clarity of the figure, only shock velocities from 100 to 300 km s^{-1} are used, and higher velocities shocks which do not match the observed [Ne ɪɪ]/[Ne ɪɪɪ] line emission ratio (see Section 5) are discarded.

The observed [Fe ɪɪ](25.99 μm)/[Ne ɪɪ](12.81 μm) and [Si ɪɪ] (34.82 μm)/[Ne ɪɪ](12.81 μm) ratios are both smaller than the shock values. The iron and silicon lines are not dominant cooling lines of ionizing shocks. The gas abundances of these elements do not impact the thermal structure of the shock, and the line intensities roughly scale with the gas phase abundances. We thus interpret the offset between the IRS observation and model values as evidence for Fe and Si depletion. We consider the magnitude of the depletions indicated by the arrow (∼50% and ∼60% for Fe and Si, respectively) in Figure 11 as lower limits, since there could be a contribution to the [Fe ɪɪ] and [Si ɪɪ] line emission from non-ionizing J-shocks into molecular gas (Hollenbach & McKee 1989). Such shocks could also contribute to the [O ɪ](6300 Å) line emission as discussed in Guillard et al. (2009). Forthcoming observations of the H$_2$ rovibrational line emission in the near-IR should allow us to estimate whether they may be significant. A contribution from non-ionizing shocks to the [Fe ɪɪ] and [Si ɪɪ] line emission will raise the depletion of both Fe and Si as well as the Fe/Si depletion ratio because non-ionizing shocks do not produce [Ne ɪɪ] line emission and the [Fe ɪɪ](25.99 μm)/[Si ɪɪ](34.82 μm) line emission ratio in J-shocks within dense gas is larger than for shocks plotted in Figure 11.

6.3. Comparison with Cold H$_2$ Distribution

A key aspect to understanding the emission we observe in SQ, as well as a test of the proposed model of H$_2$ excitation, is the amount and distribution of cold H$_2$, as measured by CO. A reservoir of cold H$_2$ associated with the warm gas observed in SQ would provide key insight into conditions within the IGM. In Figure 12, we show the BIMA array CO (1-0) integrated intensity contours from Gao & Xu (2000), shown with the H$_2$ S(0) and S(1) emission contours, overlaid on an optical image of SQ. These interferometric observations use the large primary beam of 110″, centered on the shock, to determine areas of high column densities in the group. The CO traces areas of known star formation seen at 24 μm and in the NUV (see Section 3.3), notably SQ-A and 7318b-south. As observed by Yun et al. (1997), the CO around NGC 7319 is concentrated in two regions. The dominant complex is north of the nucleus residing in a dusty tidal feature. The nuclear CO is elongated perpendicular to the
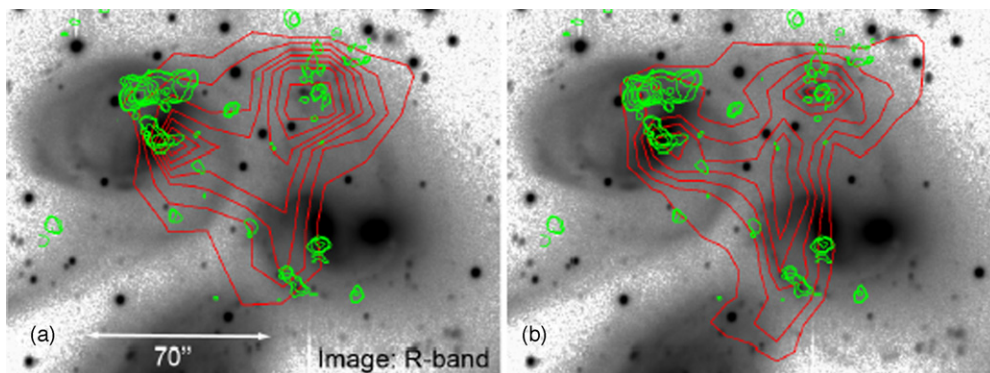
Figure 12. CO (1-0) contours (green) from Gao & Xu (2000) overlaid on an R-band image (Xu et al. 1999) of the group. Contour levels correspond to 2.4σ, 3.0σ, 4.0σ, 5.0σ, 6.0σ, 7.0σ, and 8σ (1.0σ ∼ 0.025 Jy). We show the H$_2$ contours (red) for the S(0) line (a) and the S(1) line (b) with contour levels as in Figures 2(a) and (b), respectively.

stellar disk suggesting a deficiency of ongoing star formation in the disk.

The CO distribution does not correlate with the location of warm H_2 emission, particularly around NGC 7319. The cold H_2 complexes are clearly offset from the concentrations of warm H_2. Even the S(0) emission line (see Figure 12(a)), which follows the coldest warm H_2, does not have peaks corresponding to the strongest CO detections.

In a forthcoming paper (P. Guillard et al. 2010, in preparation), we will report the recent detection of $^{12}CO(1-0)$ and (2-1) emission, associated with the warm H_2 in the SQ shock, using the single-dish 30 m IRAM telescope. These observations suggest that most of the CO emission in the shock has been missed by interferometers (because of the broad line width) and show that the CO emission is both present in the shock and extends along the H_2-emitting bridge and toward NGC 7319.

The kinematics of the CO gas lying outside of star-forming regions, in the new observations, appears to be highly disturbed with a broad line width in agreement with the Appleton et al. (2006) interpretation that the MIR H_2 lines were intrinsically very broad and resolved by the high-resolution module of IRS. The CO data also agree with our reanalysis of the Appleton et al. (2006) data (see Appendix B) using more recent and reliable wavelength calibration, which places the bulk of the H_2 gas at velocities intermediate to that of the intruder and the group—supporting the idea that the H_2 gas is accelerated in the shock.

6.4. Turbulent Suppression of Star Formation in the H_2 Filaments

Section 3.3 discussed the star-forming regions observed in SQ and noted that there was very little evidence for star formation in the shock associated with the warm H_2 emission. The main shock contains a large quantity of warm molecular hydrogen ($5.0 \times 10^8 \, M_\odot$) providing a reservoir of fuel for star formation once it cools (see Section 4). We investigate star formation in the warm H_2-dominated medium by considering the shock subregion, chosen to avoid star-forming regions in the intruder galaxy, but likely still subject to some contamination from these regions.

PAH emission is a classical tracer of star formation, but the molecules are fragile and easily destroyed in hard radiation fields. In the spectra of the main shock and subregion (Figures 8(a) and (b)), the PAH emission bands at $6.2 \, \mu m$, $7.7 \, \mu m$, and $8.6 \, \mu m$ are far weaker compared to the $11.3 \, \mu m$ bands, which when strong are predominantly produced by neutral PAH molecules (Draine & Li 2001). In the shock subregion, we find an upper limit flux for the $6.2 \, \mu m$ PAH of 0.47×10^{-17} W m^{-2} and fluxes of 0.87×10^{-17} W m^{-2} and 2.49×10^{-17} W m^{-2} for the 7.7 and $11.3 \, \mu m$ bands, respectively. This corresponds to a $7.7 \, \mu m/11.3 \, \mu m$ PAH ratio of 0.35, very low compared to the median value found for the SINGS sample of 3.6 (Smith et al. 2007).

The suppression of the $7.7 \, \mu m/11.3 \, \mu m$ PAH ratio has been observed in AGN environments (e.g., low-luminosity AGNs in the SINGS sample of Smith et al. 2007) and is favored to be the result of selective destruction of PAH molecules small enough to emit at $7.7 \, \mu m$. PAH processing in the shock due to larger molecules being less fragile than smaller ones is discussed further in Guillard et al. (2010). An alternative explanation is that the PAH molecules are chiefly large and neutral in the shock, producing enhanced $11.3 \, \mu m$ emission in comparison to the smaller PAH molecules. A detailed comparison of the dust

and PAH emission properties can be found in Guillard et al. (2010).

Dust emission in the mid- and far-infrared can be used to infer the amount of star formation taking place (Kennicutt 1998). We measure a $24 \, \mu m$ flux in this region of 0.408 mJy, corresponding to a spectral luminosity (νL_ν) of $L_{24} = 1.38 \times 10^7 \, L_\odot$. This low luminosity is consistent with the weak MIR continuum (Figure 8(b)), arising from emission from VSGs heated by the UV radiation field.

We can combine this with a measurement of the $H\alpha$ emission in this region to obtain a star formation rate (SFR), given that they are complementary ($H\alpha$ tracing the young stellar population and $24 \, \mu m$ as a measure of dust-absorbed stellar light). We find $L_{H\alpha} = 2.03 \times 10^6 \, L_\odot$, but caution that $H\alpha$ emission in SQ is also the result of shock-excitation (Xu et al. 2003) and must be considered an upper limit for measuring star formation. When we combine $L_{H\alpha}$ with L_{24}, using the relation of Calzetti et al. (2007), we find a SFR of $<0.05 \, M_\odot$ yr^{-1}.

A further measure of star formation can be obtained from the PAH strength. Using the relation of Houck et al. (2007), derived from the starburst sample of Brandl et al. (2006), we can use the $7.7 \, \mu m$ flux density as a measure of star formation. The shock subregion has a $7.7 \, \mu m$ flux density of 0.73 mJy which corresponds to a SFR of $\sim$0.08 $M_\odot$ yr^{-1}, in good agreement with our previous calculation, but also an upper limit as some PAH emission is contamination from known star formation regions in the group. A point of caution, however, is that this star formation indicator may be biased given that we detect suppressed $7.7 \, \mu m$ emission compared to the $11.3 \, \mu m$ PAH. Comparing the $L_{PAH}(7.7 \, \mu m)/L_{24}$ ratio to the galaxies in SINGS, we find that the value of $\sim$0.17 is typical of star-forming galaxies (Ogle et al. 2010), which suggests that both measures of star formation are low, but self-consistent.

The low *upper limits* for the SFR in the shock suggest that star formation is depressed in the shock apart from in the IGM starburst, SQ-A, which has a SFR of $\sim$1.25 $M_\odot$ yr^{-1} at the velocity of the group (Xu et al. 2003). This would be consistent with a picture of molecular hydrogen being reheated by MHD shocks in the turbulent medium.

Since the Jeans mass increases with gas temperature and turbulence and shearing morions will prevent collapse, the cold molecular gas clouds may be too short-lived or undersized to facilitate collapse and produce significant star formation (Guillard et al. 2009). The extent of a cold reservoir of molecular gas in the shock is a key consideration in this scenario, as discussed in Section 6.3.

7. IMPLICATIONS FOR HIGH-z GALAXY FORMATION

The present observations suggest that molecular line cooling in dense clumps dissipates a significant fraction of the kinetic energy available in high-speed shocks. For reference, and to provide a glimpse of what this group might look like at high redshift when filling a single beam, we present in Figure 13 the spectrum extracted for the entire group (i.e., including the three neighboring galaxies and the shock). The total H_2 line emission from the whole group exceeds 10^{42} erg s^{-1} and is still the most dominant MIR coolant. Indeed the luminosity of the rotational H_2 lines is sufficient that it could be detected at high redshift with future far-infrared or submillimeter instrumentation like SPICA or SAFIR (see Appleton et al. 2009). How likely is it, however, that high-speed shocks play a role in the assembly of galaxies?

There is growing evidence that galaxies at high redshift are turbulent (Förster Schreiber et al. 2006; Genzel et al. 2008)
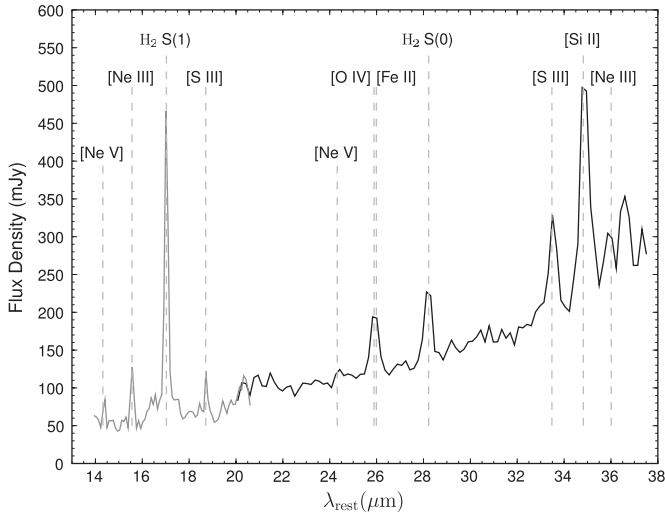
Figure 13. Low-resolution spectrum of the entire SQ region mapped by the IRS. This extraction is a rectangular box corresponding to an area of 94 kpc × 56 kpc centered on $22^h35^m59^s.97$, $+33°58'12''.7$, and includes the main shock, H₂ bridge, NGC 7319, SQ-A and NGC 7318a and NGC 7318b.

and increasingly clumpy (e.g., Conselice et al. 2005; Elmegreen & Elmegreen 2005). Indeed Bournaud & Elmegreen (2009) discuss the importance of the growth instabilities in massive gas clumps in forming disks at $z > 1$, and favor at least a large fraction of the clump systems being formed in smooth flows, perhaps similar to those discussed by Dekel et al. (2009). To what extent the build-up of these disks is truly "smooth" is not yet clear since the medium is likely to be a multiphase one. In a more standard picture, gas flowing into the more massive dark halos will experience strong shocks, most likely in an inhomogeneous medium (e.g., Greif et al. 2008)—thus, it begs the question of how important H₂ cooling may be in these different cases.

Models of the collapse of the first structures predict that strong metal lines soon dominate the cooling over molecular hydrogen when the first stars pollute the environment. It is therefore usually assumed that, except at very early stages, molecular hydrogen is a minority coolant in gas that forms the first major structures (e.g., Bromm et al. 2001; Santoro & Shull 2006). However, our observations show that, under the right conditions, even in high metallicity environments, molecular hydrogen can be extremely powerful—in this case dominating by a factor of 10 over the usually powerful [Si II]34.82 μm line in strong shocks. If there are situations at high redshift where strong shocks propagate into a clumpy, multiphase medium, then our observations imply that molecular hydrogen cooling cannot be assumed to be negligible. On the other hand, this will not be a trivial problem. Our best model of SQ (Guillard et al. 2009) involves the formation of H₂ in a complex multiphase turbulent medium in which shocks destroy dust in some places, but allow survival in others—thus encouraging H₂ formation.

In the early universe, this enhanced cooling, which has so far been neglected, will depend on the distribution and nature of the first dust grains, in concert with the formation, temperature, and abundance of gas, and the feedback effects from the first stars and AGNs.

8. CONCLUSION

In this paper, we have presented the results of the mid-infrared spectral mapping of the Stephan's Quintet system using the *Spitzer Space Telescope*. We highlight here our five main conclusions.

1. The powerful H₂ emission detected by Appleton et al. (2006) surprisingly represents only a small fraction of the group-wide warm H₂ (with a lower limit luminosity of 1.1×10^{42} erg s^{-1} spread over $\sim$975 kpc^2) that dominates the MIR emission of the system. There is evidence for another shock-excited feature, the so-called H₂ bridge between the main shock and NGC 7319, which is likely a remnant of past tidal interactions within the group. The spatial variation in the distribution of the H₂ 0-0 line ratios implies differences in temperature and excitation in the shocked system—this will be explored fully in Paper II.

2. The global $L(H_2)/L_{X(0.001-10 \text{ kev})}$ ratio in the main shock is $\geqslant$3, and $\sim$2.5 in the new "bridge" feature. The results confirm that MIR H₂ lines are a stronger coolant than X-ray emission over the shock structures, indicating a new cooling pathway seen on a large scale in SQ. This modifies the traditional view that X-rays dominate cooling at all times in the later stages of compact group evolution. Since H₂ forms on the surfaces of dust grains, we expect dust emission associated with these regions, but a low intensity radiation field produces only weak emission at 24 μm.

3. Following earlier interpretations of nebular line ratios in the optical, we interpret infrared ionic lines within the framework of fast ($V_s > 100$ km s^{-1}) ionizing shocks. Comparison between the [Ne II], [Ne III], [Si II], and [Fe II] line intensities implies that both silicon and iron are depleted onto dust. This result implies that dust is not destroyed in the shock.

4. Star formation in SQ is dominated by SQ-A and 7318b-south, located at the extreme ends of the shock ridge seen at radio wavelengths, suggesting that they are both shock-triggered starbursts. However, regions dominated by warm H₂ emission exhibit very low SFRs, consistent with a turbulent model where H₂ is significantly reheated and cool clouds are too short-lived or undersized to collapse.

5. In SQ, we observe the projected co-existence of [Si II] and H₂ being produced by $\sim$200 km s^{-1} and $\sim$20 km s^{-1} velocity shocks, respectively. Our observational results are consistent with a model of a multiphase post-shock medium produced by a galaxy-wide collision (Guillard et al. 2009).

The cooling pathway of warm H₂ emission we observe group-wide in SQ is clearly a significant, albeit surprising, mechanism in shock systems. To determine the overall dominant cooling mechanism in SQ, we require an inventory of lines and continuum processes at all wavelengths. Early shock models (Draine et al. 1983) predict that, apart from the rotational emission from H₂, contributions from lines such as [O I]63.2 μm, [C II]157.7 μm and the THz spectrum of H₂0 (Pearson et al. 1991) could be significant. We hope to explore this chemistry more fully, and the detailed distribution of cool dust, using the capabilities of the *Herschel Space Observatory*. In addition, we cannot rule out strong UV line cooling.

Stephan's Quintet provides the ideal laboratory for probing a mechanism potentially crucial in systems ranging from ULIRGs to radio galaxies to supernova remnants.
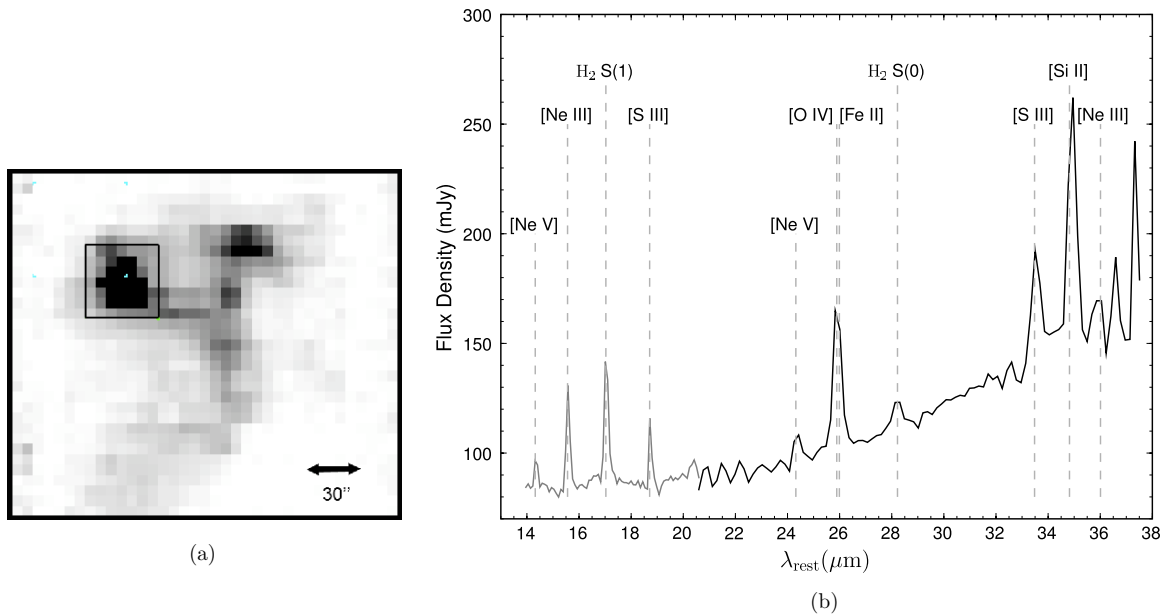
Figure 14. Rectangular extraction box for the Seyfert 2 galaxy NGC 7319 overlaid on the H_2 0-0 S(1) line emission (a) and the corresponding low-resolution spectrum (b). The extraction box is centered on $22^h36^m03^s.62$, $+33°58'35''.6$.

APPENDIX A

THE SEYFERT II GALAXY, NGC 7319

In this Section we discuss the results pertaining to NGC 7319, a Seyfert 2 galaxy (Durret 1994) lying to the East in the SQ group (see Figure 1). The specific intensity contours for the H_2 S(0) and H_2 S(1) lines (Figures 2(a) and (b)) show emission associated with the galaxy, seemingly connected to the rest of the group by the H_2 "bridge" discussed in Section 3.1. Figure 3 shows that the nucleus of NGC 7319 produces strong X-ray emission (Trinchieri et al. 2003) and is prominent at radio wavelengths (Xu et al. 2003). However, we observe an offset between the peak of the H_2 emission near NGC 7319 and the Seyfert nucleus, which suggests that the "bridge" is a separate structure and not being excited by the AGN.

The AGN in NGC 7319 does not have a well-collimated jet, but two extended lobes with compact hotspots asymmetrically distributed along the minor axis of the galaxy (Xanthopoulos et al. 2004). This structure runs northeast–southwest, and its orientation compared to the H_2 filament (which runs east–west) is not consistent with causing the excitation of the H_2 bridge. This is also evident from the relatively weak power in the AGN, as inferred by the emission-line diagnostics discussed below, and in the X-ray where it is only a factor of ~2 greater than the emission associated with the main shock and "bridge."

In Figure 4, we present the specific intensity contours of the [Fe II]25.99 μm (blended with [O IV]25.89 μm), [S III]33.48 μm, and [Si II]34.82 μm emission lines. Given the low spectral resolution of the SL and LL modules of *Spitzer*, we cannot distinguish between emission from [Fe II] and [O IV]. The AGN in NGC 7319 is likely to produce both, with [Fe II] emission likely originating in X-ray dissociation regions (XDRs) surrounding the AGN (Maloney et al. 1996). Prominent emission from [S III]33.48 μm and [Si II]34.82 μm are due to the high excitation conditions associated with the AGN. Dense PDRs and X-ray-dominated regions, powered by AGNs, show strong [Si II] emission at 34.82 μm, while [S III] 33.48 μm emission acts as a tracer of H II regions.

We now focus on the emission-line properties of NGC 7319. Figure 14 shows the spectrum extracted from the galaxy, and the measured properties of the line ratios are listed in Tables 1 and 2. For the first time in the SQ group, we observe a spectrum which is no longer dominated by H_2 emission, but instead the brightest lines are the high-excitation [O IV]25.91 μm and [Fe II]25.98 μm blended lines, as well as the [Si II]34.81 μm line. [Ne v] is prominent at both 14.32 μm and 24.30 μm—a line typically seen in AGNs. Also, unlike the majority of the extended shocked regions, there is a rising thermal continuum more typical of a star-forming galaxy than a classical Seyfert galaxy, although as various studies have shown (Buchanan et al. 2006; Deo et al. 2007), Seyfert II galaxies exhibit a variety of MIR spectral characteristics at long wavelengths. NGC 7319's rising continuum is similar to that seen in the Seyfert II galaxy NGC 3079 (Deo et al. 2007), and likely represents a dominant starburst component in the far-IR. *Spitzer* imaging reveals not only a bright nucleus, but also extended emission regions in the galaxy.

Using the [Si II]34.81 μm/[S III]33.48 μm ratio as a probe of excitation sources, we find a ratio of ~1.85 which is low compared to the average value found for AGN galaxies (~2.9) in the SINGS, but high compared to star-forming regions (~1.2) in the same sample (Dale et al. 2006). This suggests a relatively weak AGN. The [Ne III] 15.56 μm/[Ne II] 12.81 μm ratio is a measure of radiation field strength and the value of 0.97 indicates a typical radiation field strength compared to other AGNs (the sample of Weedman et al. 2005 shows a range of ~0.17 to 1.9). The average electron density, estimated from the [S III]18.71 μm/[S III]33.48 μm ratio of ~0.56, is 100–200 cm^{-3} (Martín-Hernández et al. 2002), in the low-density limit for this diagnostic (Smith et al. 2009).

The properties of the H_2 emission of NGC 7319 are limited to the two long wavelength lines observed by IRS-LL (the galaxy lies outside the region mapped by SL). As a result, the excitation diagram contains only two points allowing only an approximate idea of the H_2 mass, since without the SL wavelength coverage to provide information on possible warmer components, we are likely to overestimate the temperature of the H_2 by fitting

Table A1
X-ray Count Rates and Fluxes for Extracted Regions

Region	Count Rate (0.3–2 keV) (photons s^{-1})	Flux (0.3–2 keV) erg s^{-1} cm^{-2}	Bolometric Flux (0.001–10 keV) erg s^{-1} cm^{-2}	Adopted Spectral Model
Main shock	0.102	1.8×10^{-13}	2.8×10^{-13}	$T = 0.7$ keV
Shock sub-region	0.017	3.3×10^{-14}	5.1×10^{-14}	$T = 0.8$ keV
Bridge	0.017	3.0×10^{-14}	4.5×10^{-14}	$T = 0.6$ keV
NGC 7319	0.051	1.1×10^{-13}	3.7×10^{-13}	$\Gamma = 1.7$
SQ-A	0.013	2.4×10^{-14}	3.7×10^{-14}	$T = 0.6$ keV

Note. Statistical uncertainties on all flux measurements are <10%.
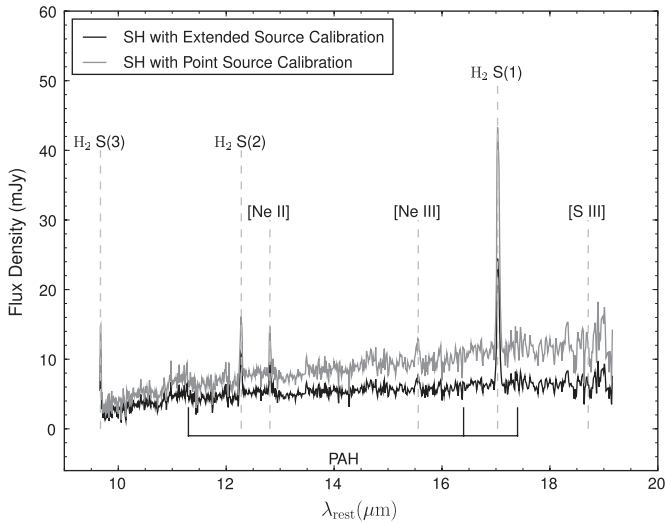
Figure 15. *Spitzer* short-high (SH) spectrum, centered on $22^{\rm h}35^{\rm m}59^{\rm s}57$, $+33°58'1''8$, reanalyzed using the latest point source and extended source calibrations.

a straight line to the points. Any warmer component would contribute to the flux of the 0-0 S(1) line thus leading to a reduction of the temperature (and increase in H₂ mass) for any cooler component. However, to provide a guide, we estimate the temperature of H₂ ⩽ 171 ± 8 K (assuming the gas is in thermal equilibrium and thus an ortho-para ratio of 2.65) and a total H₂ mass of $(3.0 \pm 7) \times 10^8 \, M_\odot$. We consider this a lower limit to the total warm mass if (as is likely) more than one component is present. Gao & Xu (2000) estimated the *cold* molecular hydrogen mass of NGC 7319 based on ^{12}CO (1-0) observations as $>3.6 \times 10^9 \, M_\odot$, a factor of roughly 10 greater than the warm H₂ mass. Such a ratio is not atypical of large spiral galaxies Rigopoulou et al. (2002).

APPENDIX B

HIGH-RESOLUTION SPECTRUM OF SHOCK CENTRE REANALYZED

The high-resolution spectrum at the center of the shock in SQ, obtained by Appleton et al. (2006), has been reanalyzed using the latest calibrations available for the IRS instrument (SSC pipeline version S17) and is included as in Figure 15. This has shown that the H₂ gas lies at a velocity of 6360(±100) km s^{-1}, between the velocity of the group (6600 km s^{-1}) and the velocity of the intruder (5700 km s^{-1}). This is consistent with a model of gas being accelerated by the shock, as well as the turbulence demonstrated by the broad line width of the H₂ in the shock (860 km s^{-1}).

The new SH spectrum shows that with the improved calibrations, the 11.3 μm PAH feature is detected, although faint. This

is consistent with what is found in the larger extractions that show enhanced 11.3 μm PAH emission compared to ionized PAH features emitting at 6.2 μm and 7.7 μm.

APPENDIX C

X-RAY FLUXES IN EXTRACTED REGIONS

In this section, we present the X-ray fluxes in the extraction regions shown in Figure 7. The reanalysis of archival data is necessary to obtain accurate fluxes and luminosities for the X-ray emission over the various apertures matched to our spectral extractions. We use the *XMM-Newton* EPIC-pn data (see Trinchieri et al. 2005, for observational details) to obtain the most sensitive measurements. A calibrated event file was generated and filtered using standard quality flags, and subsequently cleaned of background flares. A 0.3–2 keV image was then extracted and corrected for instrumental response. All point-like sources were masked out to 25″ in the analysis of diffuse emission, and the local background level was estimated within a 5 × 9 arcmin^2 rectangular region away from the group core. For each region in Figure 7, resulting background-subtracted photon count rates were converted to 0.3–2 keV and "bolometric" (0.001–10 keV) X-ray fluxes assuming an absorbed thermal plasma model of metallicity 0.4 Solar, with temperature as estimated from the map of O'Sullivan et al.(2009), and an absorbing Galactic H I column density of $N_H = 6.2 \times 10^{20}$ cm^{-2}. For NGC 7319, which harbors an AGN, an absorbed power-law spectrum of photon index $\Gamma = 1.7$ was assumed instead. Results are listed in Table A1.

We note that for the main shock (with luminosity 1.9×10^{41} erg s^{-1} in the 0.3–2 keV band), we are within a factor of 2 of the 0.5–2 keV luminosity $\sim 3.1 \times 10^{41}$ erg s^{-1} obtained for a similar, but larger extraction of the shock by Trinchieri et al. (2005). O'Sullivan et al. (2009) obtain a 0.5–2 keV surface brightness of $0.07 \, L_\odot$ pc^{-2} in the main shock compared to our value of $0.1 \, L_\odot$ pc^{-2} for the 0.3–2 keV surface brightness.

REFERENCES

Allen, M. G., Groves, B. A., Dopita, M. A., Sutherland, R. S., & Kewley, L. J. 2008, ApJ, 178, 20
Allen, R. J., & Hartsuiker, J. W. 1972, Nature, 239, 324
Allen, R. J., & Sullivan, W. T., III. 1980, A&A, 84, 181
Appleton, P. N., Charmandaris, V., Horrelou, C., Mirabel, I. F., Ghigo, F., Higdon, J. L., & Lord, S. 1999, ApJ, 527, 143
Appleton, P. N., et al. 2006, ApJ, 639, L51
Appleton, P. N., et al. 2009, Astro2010: The Astronomy and Astrophysics Decadal Survey, Science White Papers, 2010, 2 (http://www8.nationalacademies.org/astro2010/DetailFileDisplay.aspx?id=137)
Bernard-Salas, J., et al. 2009, ApJS, 184, 230
Black, J. H., & van Dishoeck, E. F. 1987, ApJ, 322, 412
Bournaud, F., & Elmegreen, B. G. 2009, ApJ, 694, L158
Brandl, B. R., et al. 2006, ApJ, 653, 1129
Bromm, V., Ferrara, A., Coppi, P. S., & Larson, R. B. 2001, MNRAS, 328, 969

Buchanan, C. L., Gallimore, J. F., O'Dea, C. P., Baum, S. A., Axon, D. J., Robinson, A., Elitzur, M., & Elvis, M. 2006, AJ, 132, 401
Calzetti, D., et al. 2007, ApJ, 666, 870
Conselice, C. J., et al. 2005, ApJ, 633, 29
Dale, D. A., et al. 2006, ApJ, 646, 161
Dekel, A., Sari, R., & Ceverino, D. 2009, ApJ, 703, 785
Deo, R. P., et al. 2007, ApJ., 671, 124
Dopita, M. A., & Sutherland, R. S. 1995, ApJ, 455, 468
Draine, B. T., & Li, A. 2001, ApJ, 551, 807
Draine, B. T., Roberge, W. G., & Dalgarno, A. 1983, ApJ, 264, 485
Draine, B. T., & Woods, D. T. 1992, ApJ, 387, 732
Durret, F. 1994, A&AS, 105, 57
Egami, E., Rieke, G. H., Fadda, D., & Hines, D. C. 2006, ApJ, 652, L21
Elmegreen, B. G., & Elmegreen, D. M. 2005, ApJ, 627, 632
Förster Schreiber, N. M., et al. 2006, ApJ, 645, 1062
Gao, Y., & Xu, C. 2000, ApJ, 542, L83
Genzel, R., et al. 2008, ApJ, 687, 59
Greif, T. H., Johnson, J. L., Klessen, R. S., & Bromm, V. 2008, MNRAS, 387, 1021
Guillard, P., Boulanger, F., Cluver, M., Appleton, P. N., Pineau des Forêts, G., & Ogle, P. 2010, A&A, submitted
Guillard, P., Boulanger, F., Pineau des Forêts, G., & Appleton, P. N. 2009, A&A, 502, 515
Hatch, N. A., Crawford, C. S., Fabian, A. C., & Johnstone, R. M. 2005, MNRAS, 358, 765
Helou, G., & Bicay, M. D. 1993, ApJ, 415, 93
Hewitt, J. W., Rho, J., Andersen, M., & Reach, W. T. 2009, ApJ, 694, 1266
Ho, L. C., & Keto, E. 2007, ApJ, 658, 314
Hollenbach, D., & McKee, C. F. 1989, ApJ, 342, 306
Hollenbach, D. J., & Tielens, A. G. G. M. 1997, ARA&A, 35, 179
Houck, J. R., Weedman, D. W., Le Floc'h, & Hao, L. 2007, ApJ, 671, 323
Houck, J. R., et al. 2004, ApJS, 154, 18
Kennicutt, R. C., Jr. 1998, ARA&A, 36, 189
Lepp, S., & McCray, R. 1983, ApJ, 269, 560
Maloney, P. R., Hollenbach, D. J., & Tielens, A. G. G. M. 1996, ApJ, 466, 561
Martín-Hernández, N. L., Vermeij, R., Tielens, A. G. G. M., van der Hulst, J. M., & Peeters, E. 2002, A&A, 389, 286

Moles, M., Sulentic, J. W., & Márquez, I. 1997, ApJ, 485, L69
Neufeld, D. A., Hollenbach, D. J., Kaufman, M. J., Snell, R. L., Melnick, G. J., Bergin, E. A., & Sonnentrucker, P. 2007, ApJ, 664, 890
Ogle, P., Antonucci, R., Appleton, P., & Whysong, D. 2007, ApJ, 668, 699
Ogle, P., Boulanger, F., Antonucci, R., Appleton, P. N., Evans, D. A., Leipski, C., & Nesvadba, N. 2010, ApJ, submitted
O'Sullivan, E. O., Giacintucci, S., Vrtilek, J. M., Raychaudhury, S., & David, L. P. 2009, ApJ, 701, 1560
Pearson, J. C., De Lucia, F. C., Anderson, T., Herbst, E., & Helminger, P. 1991, ApJ, 379, L41
Pietsch, W., Trinchieri, G., Arp, H., & Sulentic, J. W. 1997, A&A, 322, 89
Rieke, G., et al. 2004, ApJS, 154, 204
Rigopoulou, D., Kunze, D., Lutz, D., Genzel, R., & Moorwood, A. F. M. 2002, A&A, 389, 374
Santoro, F., & Shull, J. M. 2006, ApJ, 643, 26
Shull, J. M., & Hollenbach, D. J. 1978, ApJ, 220, 525
Simpson, J. P., Witteborn, F. C., Price, S. D., & Cohen, M. 1998, ApJ, 508, 268
Smith, J. D. T., et al. 2007, PASP, 119, 1133
Smith, J. D. T., et al. 2009, ApJ, 693, 713
Sulentic, J. W., Rosado, M., Dultzin-Hacyan, D., Verdes-Montenegro, L., Trincheri, G., Xu, C., & Pietsch, W. 2001, AJ, 122, 2993
Trinchieri, G., Sulentic, J., Breitschwerdt, D., & Pietsch, W. 2003, A&A, 401, 173
Trinchieri, G., Sulentic, J., Pietsch, W., & Breitschwerdt, D. 2005, A&A, 444, 697
Verma, A., Lutz, D., Sturm, E., Sternberg, A., Genzel, R., & Vacca, W. 2003, A&A, 403, 829
Weedman, D., et al. 2005, ApJ, 633, 706
Werner, M. W., et al. 2004, ApJS, 154, 1
Williams, B. A., Yun, M. S., & Verdes-Montenegro, L. 2002, AJ, 123, 2417
Xanthopoulos, E., Muxlow, T. W. B., Thomasson, P., & Garrington, S. T. 2004, MNRAS, 353, 1117
Xu, C., Sulentic, J. W., & Tuffs, R. 1999, ApJ, 512, 178
Xu, C. K., Lu, N., Condon, J. J., Dopita, M., & Tuffs, R. J. 2003, ApJ, 595, 665
Xu, C. K., et al. 2005, ApJ, 619, L95
Yun, M. S., Verdes-Montenegro, L., del Olmo, A., & Perea, J. 1997, ApJ, 475, L21